Interstellar Deuterium, Nitrogen, and Oxygen towards HZ 43A: Results from the Far Ultraviolet Spectroscopic Explorer (FUSE) Mission[1]

J. W. Kruk[2], J. C. Howk, M. Andre, H. W. Moos, W. R. Oegerle[3], C. Oliveira, K.R. Sembach, P. Chayer[4]

Department of Physics and Astronomy, Johns Hopkins University, Baltimore, MD 21218

USA

J. L. Linsky, B. E. Wood

JILA, University of Colorado and NIST, Boulder, CO, 80309-0440 USA

R. Ferlet, G. Hébrard, M. Lemoine, A. Vidal-Madjar

Institut d'Astrophysique de Paris, 98^{b}is Boulevard Arago, F-75014, Paris, France

and

G. Sonneborn

Laboratory for Astronomy and Solar Physics, NASA/GSFC, Code 681, Greenbelt, MD

20771 USA

Received _____ _____; accepted _____

---

[2]kruk@pha.jhu.edu

[3]Present address: Laboratory for Astronomy and Solar Physics, NASA/GSFC, Code 681, Greenbelt, MD 20771 USA

[4]Department of Physics and Astronomy, University of Victoria, P.O. Box 3055, Victoria, BC V8W 3P6, Canada

version 11/19/2001

ABSTRACT

We present an analysis of interstellar absorption along the line of sight to the nearby white dwarf star HZ 43A. The distance to this star is 68 ± 13 pc, and the line of sight extends toward the north Galactic pole. Column densities of O I, N I, and N II were derived from spectra obtained by the Far Ultraviolet Spectroscopic Explorer (*FUSE*), the column density of D I was derived from a combination of our *FUSE* spectra and an archival *HST* GHRS spectrum, and the column density of H I was derived from a combination of the GHRS spectrum and values derived from *EUVE* data obtained from the literature. We find the following abundance ratios (with 2σ uncertainties): D I/H I $= (1.66\pm0.28)\times10^{-5}$, O I/H I $= (3.63 \pm 0.84) \times 10^{-4}$, and N I/H I $= (3.80 \pm 0.74) \times 10^{-5}$. The N II column density was slightly greater than that of N I, indicating that ionization corrections are important when deriving nitrogen abundances. Other interstellar species detected along the line of sight were C II, C III, O VI, Si II, Ar I, Mg II, and Fe II; an upper limit was determined for N III. No elements other than H I were detected in the stellar photosphere.

Subject headings: ISM: abundances—ISM: clouds—stars: individual (HZ 43A)—stars: white dwarfs

1. Introduction

Deuterium is one of the primary products of big bang nucleosynthesis (BBN), and its primordial abundance provides a sensitive measure of the baryon density of the universe (Schramm & Turner 1998; Burles 2000). However, deuterium is consumed in stars far more quickly than it is produced by the P-P cycle or by any other known stellar nucleosynthetic

process (Epstein et al. 1976); thus, measurements of the deuterium abundance at the present epoch can only provide lower limits to the primordial abundance. Measurements obtained at a variety of redshifts will sample the chemical evolution of the universe, and may permit extrapolation to a value for the primordial abundance of deuterium. Measurements of the abundance of deuterium and various products of stellar nucleosynthesis, such as oxygen, within our Galaxy will improve our understanding of chemical evolution as well as provide a lower limit to the primordial deuterium abundance. Recent reviews of deuterium abundance measurements can be found in Lemoine et al. (1999), Linsky (1998), and Moos et al. (2001).

Linsky (1998) reviews measurements of the deuterium abundance for material in the local interstellar cloud (LIC), which are consistent with a common value for D/H of $(1.5 \pm 0.1) \times 10^{-5}$. The LIC and other nearby clouds are thought to be embedded in a large bubble of hot, low density gas ($T \approx 10^6 K$, $n \approx 0.005 \, cm^{-3}$) that was probably produced by supernovae and stellar winds arising in the Scorpius-Centaurus OB association (Cox & Reynolds 1987; Frisch 1995). If this picture is correct, then the local interstellar medium (LISM) may contain an inhomogeneous mixture of clumps of older material swept up by the expanding bubble along with the more-recently processed material in the bubble itself. Thus, even in this local environment one may find regions of gas with somewhat different evolutionary histories and different compositions. The same processes have been at work throughout the history of the Galaxy; hence measurements of deuterium and other abundances along numerous lines of sight will help determine not only the chemical evolution of the Galaxy, but also the relative timescales for chemical evolution and the mixing of material.

In this paper we present an analysis of the line of sight to the nearby white dwarf HZ 43A. Companion papers will present similar analyses of the lines of sight to G 191-B2B (Lemoine et al. 2001), WD 0621-376 (Lehner et al. 2001), WD 1634-573 (Wood et al. 2001),

WD 2211-495 (Hébrard et al. 2001), BD +28° 4211 (Sonneborn et al. 2001), and Feige 110 (Friedman et al. 2001). An overview will be provided by Moos et al. (2001).

High-resolution spectra of the DA white dwarf HZ 43A, covering the far ultraviolet (FUV) wavelength range 905–1187Å were obtained with the *Far Ultraviolet Spectroscopic Explorer* (*FUSE*) for the purpose of studying the deuterium abundance of the local interstellar medium (ISM). This line of sight is promising for a study of D/H for several reasons: the star itself is moderately bright, exhibits a nearly featureless continuum, and has been accurately modelled; the absorbing interstellar gas appears to have only a single velocity component and the column density is very low, so many absorption lines that are ordinarily on the flat part of the curve of growth are either unsaturated or exhibit only mild saturation effects. In addition, the H I column density along the line of sight can be determined by two independent methods: from the shape of the Lyman continuum observed by the *Extreme Ultraviolet Explorer* (*EUVE*), and from the Lyman-α profile observed with the Goddard High Resolution Spectrograph (GHRS) onboard the Hubble Space Telescope (*HST*). Systematic uncertainties in determination of H I column densities are often the limiting factor in measurements of the D/H ratio, so the availability of multiple independent measurements of N(H) is quite valuable.

In Section 2 we discuss the line of sight to HZ 43A and the properties of the star; in Section 3 we describe the observations and data reduction procedures; in Section 4 we describe our analysis procedures, our methods for minimizing systematic errors, and our measured column densities; and in Section 5 we summarize our results.

2. Line of Sight and Stellar Properties

The hot DA white dwarf HZ 43A (WD 1314+293) is a member of a non-interacting binary system with a dMe star. The cool secondary star has no significant UV flux. The coordinates of the star and some other basic characteristics are given in Table 1. The Galactic coordinates, $l = 54.10°, b = +84.16°$, are close to the north Galactic pole and the line of sight exits the LIC after traversing a very short distance: ~ 0.1pc (Redfield & Linsky 2000). The mean H I density in the LIC is $0.1 \, \text{cm}^{-3}$ (Linsky et al. 2000), so the corresponding column density is only $\approx 3.1 \times 10^{16} \, \text{cm}^{-2}$. The velocity of the LIC projected onto the HZ 43A line of sight is -8.9 km s^{-1} (all velocities given in this paper are heliocentric). The line of sight may intersect the "G" cloud that lies between us and the Galactic center, and the "NGP" cloud that lies between us and the North Galactic Pole (see Sfeir et al. 1999 and the review by Frisch 1995 for a discussion of the geometry of the nearby clouds lying within the local bubble). The boundaries of the clouds are not known in detail, but the identity of each absorber can be determined by its relative velocity. In particular, the velocity of the G cloud projected onto the HZ 43A line of sight is -12.1 km s^{-1}. The distance to HZ 43A has been determined by several methods to be approximately 65pc. Vennes et al. (1997) obtained 67pc from a comparison of its apparent and absolute V magnitude (derived from a model atmosphere), while Dupuis et al. (1998) obtained a somewhat smaller value, 56-61pc using a similar method. Ground-based parallax measurements have given 48-91pc (Margon et al. 1976), 53-83pc (Dahn et al. 1982), and 55-81pc (van Altena et al. 1995). The only discrepant measurement, 25 - 44pc, is from the Hipparcos catalog (Clark & Dolan 1999); the origin of this discrepancy is not understood. The apparent line-of-sight velocity of the star (including gravitational redshift) was measured by (Reid 1996) to be +20.6 km s^{-1}.

The atmospheric parameters of HZ 43A are difficult to measure at visible wavelengths, because of the presence of the bright M star companion only $\sim 3''$ away. Napiwotzki et al.

(1993, N93 hereafter) and Finley et al. (1997, FKB hereafter) obtained optical spectra of both components and corrected the observed flux of the white dwarf by subtracting the contribution from the M star. N93 obtained $T_{\rm eff} = 49,000$ K and $\log g = 7.7$ using NLTE models, while FKB determined $T_{\rm eff} = 50,800$ K and $\log g = 7.99$ using LTE models. According to Napiwotzki et al. (1999), the difference between both studies may illustrate the correction in $T_{\rm eff}$ and $\log g$ that one must apply to transform the atmospheric parameters determined by LTE models to NLTE models. However, if we apply the Napiwotzki et al. (1999) correction ($\Delta \log g = -0.13$) to FKB's value (7.99), we obtain a larger gravity than N93 (7.7).

Other spectral bands have been used to evaluate the effective temperature and gravity of HZ 43A. For example, Holberg et al. (1986) fitted the *IUE* Lyman-α line profile, obtaining a larger temperature and gravity than the optical observations performed by N93 and FKB. Both Vennes (1992) and FKB indicated that the visual magnitude estimated by Holberg et al. (1986) was too faint. The visual magnitude is quite difficult to determine from the ground because of contamination by the companion star. If Holberg et al. (1986) had used the magnitude determined from *HST* data by Bohlin et al. (1995), the effective temperature would have been $T_{\rm eff} = 50,850$ K, very close to that determined later by FKB. The complete Lyman series of HZ 43A was analyzed by Dupuis et al. (1998) using *ORFEUS* and by Kruk et al. (1997) with the *Astro-1 Hopkins Ultraviolet Telescope*, while the EUV wavelength range was studied by Dupuis et al. (1995) and Barstow et al. (1995) using *EUVE*. If we take the average of the effective temperature and gravity for all measurements made from EUV, FUV, and optical observations, we obtain $T_{\rm eff} = 50,300$ K and $\log g = 7.88$, with standard deviations of 700 K and 0.15 dex (see, e.g., Table 1 of Dupuis et al. 1998).

For the purpose of this study, we adopted the following atmospheric parameters: $T_{\rm eff} = 50,900$ K, and $\log g = 8.0$. These are the pre-publication values of FKB used by

Kruk et al. (1999) in the final *Astro-2* calibration of the *Hopkins Ultraviolet Telescope*, and used presently in the *FUSE* calibration (the present *FUSE* flux calibration is defined by HZ 43A, G 191−B2B, and GD 246).

HZ 43A is unusual in that its photosphere appears to consist entirely of hydrogen, though stars with similar atmospheric parameters show traces of heavy elements. Barstow et al. (1995) set an upper limit on the helium abundance of 10^{-7}, based on the *EUVE* spectrum of this star, and Dupuis et al. (1998) used an *ORFEUS* spectrum to set abundance limits of 10^{-7} for S, 10^{-8} for C and N, and $10^{-8.5}$ for Si, P, and Cl. Vennes et al. (1991), N93, and Dupuis et al. (1995) came to the same conclusion, though with somewhat higher upper limits. Therefore, photospheric models for this star employing a pure hydrogen composition should give accurate results.

3. Observations

3.1. *FUSE* Observations

FUSE comprises four independent co-aligned telescopes and spectrographs. Two of the channels contain optics coated with aluminum and overcoated with LiF, and the other two channels contain optics coated with SiC. Together the four channels span the wavelength range 905-1187Å. Most wavelengths in this band are sampled by at least 2 channels, and roughly one-third of the bandpass is sampled by 3 or 4 channels (1000Å $< \lambda <$ 1080Å). Comparison of features in the spectra obtained in different channels can thus be used to test for the effects of fixed-pattern noise, backgrounds, or other instrumental characteristics that vary from one channel to another. Each spectrograph has 3 entrance apertures: LWRS (30″× 30″), MDRS (4″× 20″), and HIRS (1.25″× 20″). Each aperture illuminates different regions of the detector and produces spectra with slightly different line-spread

functions (LSFs). Thus, if a source is observed through multiple apertures one can perform additional tests for the presence of fixed-pattern noise introduced by the detector, and one can determine if contamination by geocoronal emission is significant. Further information on the *FUSE* satellite and instrument on-orbit characteristics are provided by Moos et al. (2000) and Sahnow et al. (2000).

Three *FUSE* observations of HZ 43A have been obtained, two in the LWRS aperture and one in the MDRS aperture. Basic information for the datasets is given in Table 2. The data were obtained in "histogram" mode, in which a two-dimensional spectral image is accumulated and downlinked. The LWRS observations will be described here for the sake of completeness: the signal-to-noise of the LWRS observations was too low in comparison with the MDRS data for them to significantly constrain the results. They were useful primarily for tests of fixed-pattern noise effects. Exposure durations for the LWRS observations ranged from just under 500 s to just over 800 s. The exposures in the MDRS observation were all approximately 485 s, apart from a few exposures that were shortened to roughly 200 s by delayed target acquisitions. The MDRS observation was split into 4 intervals of approximately equal exposure time, each with a different X-position of the Focal Plane Assemblies (FPAs). The shift in FPA position causes a corresponding shift in the position of the spectrum on the detector along the dispersion direction. The 4 positions were at X = -57 μm, 0 μm, +33 μm, and +125 μm with respect to the nominal position, corresponding to spectral shifts of roughly -12, 0, +5, and +19 pixels. These shifts span a range several times larger than the width of typical interstellar absorption lines, and several times larger than the width of the high-frequency components of the detector fixed-pattern noise. This so-called "focal-plane split" ("FP-split") procedure results in a considerable improvement in the signal-to-noise ratio achieved, even if the the spectra from the different FPA positions are simply shifted and added with no attempt to explicitly solve for the detector fixed-pattern noise.

The data were processed using the most recent version of the *FUSE* calibration pipeline, CALFUSE version 1.8.7. Because there is no information available for the arrival time of individual photons in histogram mode, the pipeline applies exposure-averaged corrections for the Doppler shift induced by the spacecraft orbital motion and for the rotation of the gratings on orbital timescales. The primary mirrors also rotate slightly on orbital timescales, which can lead to significant changes in the position of the image of the source at the spectrograph entrance aperture. As a result, the effective spectral resolution can vary from one exposure to another and the zero-point of the wavelength scale varies from one exposure to another.

The rotations of the primary mirrors during an exposure can cause the stellar image to fall outside of the corresponding spectrograph aperture, resulting in loss of signal in that channel for all or part of an exposure. The Fine Error Sensor presently used to provide pointing information to the satellite attitude control system is part of the optical path in the LiF1 channel; hence the target is always maintained at a fixed position in the LiF1 spectrograph aperture. The alignment of the other channels is usually maintained so that the rotations of the primary mirrors occurring on orbital timescales do not shift the source image at each focal plane out of the corresponding LWRS aperture. For the M1010501 observation, no flux was lost in any of exposures; for P1042301 no flux was lost except that the SiC1 channel fluxes were low by 7%, 10%, and 19% in exposures 13, 16, and 20, respectively. The SiC1 spectra obtained in these exposures were scaled accordingly before being combined with the other exposures. For MDRS observations, peakups are performed twice in each orbit in order to try to correct for the mirror rotations by moving the spectrograph apertures (FPA)s in the dispersion direction to maximize the signal prior to the start of an exposure. For the P1042302 MDRS observation, this procedure was fairly successful, providing effective exposure times of 82% for LiF2, 62% for SiC1, and 76% for SiC2. The necessity of moving the FPAs to compensate for rotations of the primary mirrors

means that there is actually a distribution of FPA positions clustered about the mean offsets that define the FP split sequence described above.

The spectra obtained in different exposures generally need to be co-aligned (shifted to a common wavelength zero-point) prior to combining. This is caused in part by the lack of corrections for primary mirror rotations in the present pipeline, and in part by shortcomings in the present corrections for grating rotations. For HZ 43A there are no narrow photospheric lines and very few strong interstellar absorption lines. For the LiF channels, we fit a Gaussian profile to the interstellar C II 1036.337Å line in each exposure and shifted each exposure to locate this line at a common velocity. For the SiC channels, we performed a cross-correlation on the the interstellar Lyman lines between 915Å and 930Å (fitting the C II 1036.337Å line gave essentially identical results). In order to have enough signal to measure line positions, we discarded spectra for which the flux was below half of the nominal value for its channel.

3.2. GHRS Observations

Archival HST/GHRS spectra were used to determine the velocity structure of the intervening gas and to measure Lyman-α absorption of both H I and D I. A log of the GHRS observations is given in Table 3. All of the data were acquired after the installation of the Corrective Optics Space Telescope Axial Replacement (COSTAR) unit. The echelle-mode data, all of which were acquired through the large science aperture (LSA; $1.74'' \times 1.74''$), have a line spread function with a narrow core of resolution 3.5 km s^{-1} (FWHM) and broad wings ($\sim$15 km s^{-1} FWHM) with relatively low power (see Appendix B of Howk et al. 1999).

Our reduction of these data follows that of Howk et al. (1999). The basic calibration

makes use of the standard CALHRS pipeline with the best calibration reference files available as of the end of the GHRS mission. The CALHRS processing includes conversion of raw counts to count rates and corrections for particle radiation contamination, dark counts, known diode nonuniformities, paired pulse events and scattered light. The wavelength calibration was derived from the standard calibration tables based upon the recorded grating carrousel position. The absolute wavelength scale should be accurate to $\sim$1 resolution element, or $\sim$3.5 km s^{-1} for the echelle-mode data used in this work.

All of the echelle-mode observations employed here were taken at four separate grating carrousel positions to place the spectrum at different positions along the 500-diode science array of the GHRS. This is done to mitigate the effects of the fixed-pattern noise that can limit the signal-to-noise ratio and produce artifacts in GHRS spectra. We have co-added each of the individual sub-exposures by aligning the interstellar lines of interest (e.g., D I, Mg II, and Fe II) in each of the observations. We used the algorithm of Cardelli & Ebbets (1994) to explicitly solve for the fixed-pattern noise spectrum in each of the datasets. However, we found it unnecessary to apply this correction because the signal-to-noise ratio of the data did not necessitate the removal of the low-power features and no prominent features were found (see discussion in Howk et al. 2000). We note that the coaddition of the shifted datasets reduces the strength of any fixed-pattern features by a factor of four.

The inter-order scattered light removal in GHRS echelle-mode data discussed by Cardelli et al. (1990, 1993) is based upon extensive pre-flight and in-orbit analysis of GHRS data and is used by the CALHRS routine. The coefficients derived by these authors are appropriate for observations made through the small science aperture (SSA). Corrections to these coefficients are often required to bring the cores of strongly saturated lines observed through the LSA to the correct zero level. Typically this is done by adjusting the spectrum zero level by an amount equal to a fraction of the average net flux in each order. This "d"

coefficient (Cardelli et al. 1990, 1993) accounts for the residual effects of the local echelle scattering.

For the Ech-B data covering Mg II and Fe II, no strongly saturated lines were available for evaluating the quality of the background removal, so we adopted the standard d-coefficients from the CALHRS processing. The Lyman-α absorption profile for HZ 43A should be flat-bottomed at zero flux near line center. Although the presence of strong Lyman-α airglow confuses the matter somewhat, it is clear that the use of the standard d-coefficient (d=0.052) over-subtracts the core of the Lyman-α profile. We have used the observed flux level over the wavelength range 1215.74 to 1215.83Å, assuming this represents the true zero point, to adjust the d-coefficient. The adopted d-coefficient is d = -0.006±0.033.

The G160M observations of the 1192–1228Å range were acquired through the Small Science Aperture (0.22"×0.22"; SSA). These data have a resolution of $\sim$19.6 km s^{-1} (FWHM). The scattered light properties of this holographically–ruled first–order grating are excellent. No corrections to the CALHRS background subtractions were necessary.

4. Analysis

4.1. Method

We attempted to determine column densities by more than one method whenever possible. The two primary methods were profile fitting and curve-of-growth analyses. These two methods differ in their sensitivity to some of the sytematic uncertainties that affect column density measurements. A curve-of-growth analysis was not feasible for H I, as essentially all of the lines other than Lyman-α are on the flat part of the curve of growth. Instead, H I column density measurements based on fits to the EUV spectrum of HZ 43A

were taken from the literature to provide a consistency check on our results.

Profile fitting was used to determine the column densities of H I, D I, O I, and N I. The profile fitting was performed using the program Owens.f, written by one of us (M.L.). This program uses χ^2 minimization to adjust temperatures, turbulent velocities, and relative velocities for multiple gas components, to adjust column densities for each species present in each gas component, and to adjust polynomial fits to continuum fluxes, line spread functions, background levels, etc. for each specified spectral region. Each quantity can be adjusted by the program or held fixed to user-specified values. Further information on this program is provided in the companion paper by Hébrard et al. (2001).

The *FUSE* and GHRS spectra were normalized prior to fitting by means of an NLTE stellar model. The continuum in the vicinity of individual absorption lines was then fit by a low-order polynomial as required to account for any residual flux calibration errors or flat-field effects. We use the program TLUSTY (Hubeny & Lanz 1995) to calculate the atmospheric structure of HZ 43A under the assumption of NLTE, and then we compute the detailed emergent flux using the program SYNSPEC (Hubeny 2000, private communication). The hydrogen line profiles are obtained from the Stark broadening tables computed by Lemke (1997) using the program of Vidal et al. (1973). We use a NLTE model atmosphere to calculate the emergent flux, because NLTE effects are important in the core of the Ly α line, which is formed high in the atmosphere where departure from LTE is significant (see, e.g., Wesemael et al. 1980). The model parameters used were as discussed in Section 2: the composition was pure hydrogen, $T_{eff}= 50900$K, and $\log g= 8.00$. The model spectrum was then normalized to V = 12.914 (Bohlin et al. 1995). Except for NLTE effects in the narrow cores of the Lyman lines it is essentially identical to the LTE model described in detail by Kruk et al. (1999) and references therein.

The Lyman-α profile was also fit using a different program written by one of us

(J.C.H), and the profile fitting code of Ed Fitzpatrick (Spitzer & Fitzpatrick 1993) was used to provide a consistency check for certain test cases.

We have derived column densities for N I and O I by fitting the measured equivalent widths with a single-component Gaussian (Maxwellian) curve of growth (Spitzer 1978; Jenkins 1986). The analysis was performed using software adapted from that described by Savage et al. (1990), which varies the Doppler parameter, b, and column density so as to minimize χ^2 between the observed equivalent widths and a model curve of growth. The stellar continuum in the vicinity of each line was estimated using a low-order Legendre polynomial fit to the data. The dispersion of the data about the fit was used to estimate the uncertainties in the final integrated equivalent width measurements as discussed by Sembach & Savage (1992). This estimate includes contributions from both Poisson noise and uncorrected high-frequency fixed-pattern detector features. The measurement uncertainties quoted include contributions from this noise estimate, uncertainties in the Legendre fit parameters (Sembach & Savage 1992), and estimates of the systematic uncertainties inherent in the continuum placement and velocity integration range. Atomic data for both the profile fitting and the curve of growth analysis were taken from Morton (1991, Morton 2001, private communication).

The integrated equivalent widths for several interstellar species are presented in Table 4, and the results from the curve-of-growth fits are given in Table 5. For most species other than N I and O I the number of available transitions was insufficient to fit a curve of growth and determine a b-value; instead, the measured equivalent width was combined with a curve of growth computed using the O I b-value to derive the column density. For these cases the table also lists the difference between the column density derived in this manner and that derived using a straight integration of the apparent column density profiles (Savage & Sembach 1991), providing a measure of the saturation correction.

4.2. Systematic Uncertainties

Column density determinations are subject to numerous possible systematic uncertainties. These are described in the following section, along with brief descriptions of how these were addressed. The magnitude of each effect on the column densities will then be addressed in the discussion of each species as appropriate.

4.2.1. Overlapping velocity components along the line of sight

One of the major difficulties typically encountered in measuring column densities is accounting for overlapping absorption profiles resulting from clouds with similar velocities. As we will show below, there appears to be only a single absorption component along the line of sight to HZ 43A, so this complicating factor is not present.

4.2.2. Narrow absorption features in the stellar spectrum

Stellar photospheres ordinarily contain trace quantities of numerous elements that can give rise to narrow absorption features in the emergent spectrum. In some cases the stellar spectrum is well-understood and the presence of such narrow features can be predicted and possibly even modelled. In other cases, the wavelengths of the various transitions are poorly known and it is impossible to be certain how much of an absorption profile is due to interstellar gas and how much results from the photospheric spectrum. However, as discussed in Section 2, the atmosphere of HZ 43A appears to be composed solely of hydrogen. Thus, this potential complicating factor is also not a concern for our analysis of HZ 43A.

4.2.3. Uncertainties in the stellar Lyman-α profile

The high gravity of HZ 43A causes the photospheric Lyman lines to be quite broad, hence the stellar spectrum is varying slowly in the vicinity of all of the interstellar lines being fit other than H I Lyman-α. Because we are fitting the damping wings of the interstellar H I Lyman-α profile, spanning roughly 6Å, we need to be able to model the photospheric absorption very accurately. In addition, the H I column density along the line of sight to HZ 43A is sufficiently low, and the relative velocity of the star and interstellar gas is sufficiently high, that the NLTE core of the photospheric Lyman-α profile may affect the red wing of the combined profile. HZ 43A has been studied in great detail, however, and model atmospheres and synthetic spectra of HZ 43A, along with those of several similarly well-studied DA white dwarfs, are used to define the flux calibration for most orbiting UV spectrometers (Bohlin 2000, and references therein). The parameters describing HZ 43A are discussed in Section 2, and the fits to the Lyman-α profile are discussed in Section 4.3.2.

4.2.4. Continuum placement errors

Errors in placement of the continuum or the background will clearly affect the column density determination. In most regions of the spectrum the continuum appears to be smooth and slowly-varying in the vicinity of each of the lines measured. If the continuum did not appear to be well-behaved, most likely because of large-scale fixed-pattern noise effects in the detector, then the the affected line was not included in the fit (the SiC1B MDRS measurement of the O I 948.686Å line is such a case). Uncertainties in continuum placement are included explicitly in the equivalent width measurements used in the COG analysis, and implicitly in the χ^2 minimization performed by the profile fitting. This latter approach is adequate if the true continuum is in fact well-represented by a low-order polynomial, and if the absorption being measured occupies a small fraction of the region being fit. For the

broad Lyman-α profile a variety of continuum fits were tested to determine the sensitivity of the results to the adopted continuum. This will be discussed in greater detail below in the section on the measurement of the H I column density.

4.2.5. Background placement errors

The dominant background for *FUSE* spectra of a bright source such as HZ 43A is grating scattering of source flux. The intrinsic detector background and diffuse stray light in the spectrograph are negligible in comparison. The grating-scattered source flux has been characterized by measuring the flux in the cores of highly-saturated H_2 absorption line profiles in the spectra of stars with translucent clouds along the line of sight. Typical results for this background are that the level is about 1% of the continuum flux in the SiC channels, and 0.3% to 0.5% of the continuum flux in the LiF channels. In the HZ 43A *FUSE* observations, the flux shortward of the Lyman limit is indeed about 1% of the continuum flux in the SiC1B channel. None of the interstellar absorption lines in the HZ 43A spectrum are broad enough for the true background level to be seen in the line cores. The instrumental LSF has a broad component that has a FWHM of about 18 pixels, which is broad enough that even the H I Lyman line cores do not reach the level of the background. This point is discussed further in Section 4.2.8. The effects of uncertainty in the background level were investigated by performing the profile fits with the background level set to zero, set to our best estimate of the background, and and set to twice our best estimate of the background. The resulting column density variation was typically 0.01 dex, and is included in the quoted uncertainties for the column densities. The background effects in the GHRS spectra are discussed in the section below on the H I column density measurement.

4.2.6. Geocoronal emission

Contamination of the spectrum by geocoronal emission can be significant for the large spectrograph apertures employed by *FUSE*. Such emission is quite strong at Lyman-β, but declines rapidly in strength for the higher Lyman lines. Geocoronal emission is also present on the day side of the orbit for many of the same O I and N I transitions for which we are trying to measure interstellar absorption. The widths of geocoronal lines are limited by the size of the spectrograph apertures. For the LWRS aperture this width is typically 0.35Å, or the equivalent of 106 km s^{-1} at Lyman-β, while for the MDRS aperture this width is about 0.045 Å, or the equivalent of 13 km s^{-1} at Lyman-β.

The MDRS aperture is sufficiently narrow ($\sim$13 km s^{-1}) that the geocentric velocity of the interstellar gas shifts the geocoronal emission almost completely away from narrow lines. The red wing of the broad interstellar Lyman-β line is filled in by geocoronal emission, but no difference is seen in the O I or N I absorption profiles when the day and night data are analyzed separately. The absorption profiles measured in the LiF1 channel are actually deeper for the day data than the night data, presumably because the LiF1 grating is more stable in the day than in the night and the effective resolution is correspondingly better.

4.2.7. Uncorrected fixed-pattern noise

Uncorrected fixed-pattern noise on small scales can lead to significant errors in the shapes and fluxes of line profiles; on larger scales it can lead to continuum placement errors. The *FUSE* detectors exhibit significant fixed-pattern noise on both small and large scales, caused primarily by the inherent granularity of the microchannel plates (MCPs). The slowly-varying relative spacing of the pores in the stack of 3 MCPs gives rise to Moire fringe effects with a spacing of 8-9 pixels, comparable to the width of the LSF. Changes in

pore spacing at fiber bundles and regions of dead pores can cause changes in the detector quantum efficiency on larger scales. The present CALFUSE pipeline flags pixels affected by dead regions of the detector, but otherwise fixed-pattern features are not yet corrected.

We have mitigated the effects of fixed-pattern noise by several means. Every transition being examined in the *FUSE* bandpass is sampled by either 2 or 4 channels, so we have verified that each such measurement provided essentially similar results. In addition, because HZ 43A was observed in both LWRS and MDRS apertures, we have checked for consistency of the results. The MDRS data were obtained with an FP-split procedure, which substantially reduces the fixed-pattern noise on scales of one to two resolution elements. The resulting spectra typically have a S/N that is about 80-90% of that expected from photon statistics, depending on the size of the region examined, primarily because the larger-scale fixed-pattern noise has not been removed. However, most of these fluctuations are slowly varying and can be removed by low-order polynomial fits to the continuum in the vicinity of absorption lines of interest.

4.2.8.   Uncertainties in the instrumental line spread function

Characterization of the *FUSE* LSF is still in a preliminary state. There appears to be both a narrow and a broad component to the LSF. The narrow component is somewhat wavelength-dependent and is sensitive to the accuracy of the correction for grating motion during exposures and to the accuracy with which the user was able to co-align the spectra from each exposure prior to combining them. In addition, data acquired in histogram mode cannot be corrected for the degradation of the spectral resolution caused by rotation of the primary mirrors or gratings during an exposure. For example, in some channels the resolution is better during the night portion of the orbit and for other channels it may be better during the day. As a result, the effective width of the narrow component of the LSF

will vary from one observation to another. We measured the effective width of this narrow component by fixing the temperature and turbulent velocity of the interstellar gas to that found from the GHRS measurements (see below), and letting the LSF widths vary in the profile fits. The results were generally consistent from one absorption line to another, and were typically about 9 pixels FWHM (corresponding typically to 0.062Å in the LiF channels and 0.057Å in the SiC channels). This is consistent with what is found from other FUSE datasets. These widths were then held fixed when performing subsequent fits. It should be noted that the LSF width is significantly greater near the edges of the detector active area, as are the uncertainties in the wavelength calibration.

The broad component of the LSF appears to be somewhat less sensitive to the effects of grating rotation, primary mirror rotation, or coalignment of spectra. The initial characterization the available data indicates that about 30 percent of the area of the LSF is in a component with a width in the range of 17-24 pixels. Analysis of highly saturated lines that are flat-bottomed over regions of 150 pixels or more reveals that there is no significant component of the LSF with a characteristic width larger than 25 pixels. The effects of this broad component of the LSF on the profiles of unsaturated lines may not be evident unless the signal-to-noise ratio of the data is very high; however, its main effect is to introduce a substantial apparent increase in the background under the line. If a weak line is fit with a single, narrow, Gaussian LSF, the background level in the fit must be increased to account for this effect In the profile-fitting analysis of the HZ 43A ISM absorption we have represented the LSF as a two-component Gaussian function. The width of the narrow component was determined to be about 9 pixels as described in the previous paragraph, and the broad component width was set to 17 pixels, with an amplitude corresponding to 30% of the total area.

If the LSF has very long shallow tails that cannot be distinguished from the continuum,

then both the profile fitting technique and curve-of-growth analysis would likely be subject to continuum placement errors that will cause some of the area of the line to be missed and therefore cause the the column density to be underestimated. However, while there is a component of the LSF that has roughly twice the width of the narrow component, there is no component with very long extended tails. In the absence of such a weak and very broad component, the curve-of-growth analysis is independent of the shape of the LSF, and thus provides a valuable check that the profile fit was not adversely affected by errors in the assumed LSF.

The LSF of the GHRS modes used here is smaller than the Doppler widths of the lines being measured, other than for Fe II, so there is no significant systematic error associated with uncertainties in this LSF. The Doppler width of the Fe II 2382.765Å line is comparable to the LSF width, so the determination of the Doppler width for this line does have relatively large uncertainties. The column density, however, is not adversely affected because the line is so weak.

4.2.9.   Uncertainties in the f-values

Errors in the atomic data used in the fits have the potential of biasing the results. If such errors are distributed randomly then the use of numerous lines will minimize any systematic bias of the overall column density determination. If the oscillator strengths for a given species are all too large or too small then the estimate for the column density will be biased. However, such a systematic error in the f-values seems unlikely to result in a consistent fit to all of the lines, especially if lines are included that are not on the linear part of the curve of growth. We have tested for effects on the derived column density resulting from errors in the f-values by repeating the profile fits after removing each transition and verifying that the derived column density did not vary by more than $1\,\sigma$. An examination of

the curve-of-growth plots also shows that a satisfactory fit can be obtained that is consistent with each of the included points. The only transition that was found to have an f-value clearly inconsistent with those of the other transitions was the that of the O I 1026.473Å line (see Sembach 2000). This line was excluded from all fits and from the curve-of-growth analysis.

4.3. Results

4.3.1. Line of sight velocity structure

The velocity structure of absorbing gas along the line of sight was determined from GHRS observations of D I 1215.339Å, Fe II 2383.765Å, Mg II 2796.352Å, and Mg II 2803.531Å line profiles. These lines are well-resolved, and are isolated from any other absorption features. We obtained a satisfactory fit to the lines with a single absorption component with a heliocentric velocity of -5.2 ± 0.1km s^{-1}, a temperature of T = 5353 ± 948 K, and a non-thermal velocity of b_{nt} = 2.0 ± 0.2km s^{-1} (the uncertainties are 1 σ statistical uncertainties; the systematic uncertainty on the absolute velocity is ± 3 km s^{-1}). The total Doppler parameter, b, is related to the temperature and non–thermal velocity parameter such that $b^2 = 0.0165\,T/A + b_{nt}^2$. The observed profiles and the best model fits are shown in Figure 1. There is no evidence for an additional velocity component. These values for T and b_{nt} were not held fixed in subsequent fits (e.g. for O I or N I). Instead, the derived Doppler widths for each species were computed and compared with the ranges allowed by the above values; in each case the derived Doppler widths were found to be consistent with the 1 σ uncertainties quoted above. The b-values for O I and N I predicted from the values of T and b_{nt} given above are: b(O I) = 3.1 ± 0.2 km s^{-1}and b(N I) = 3.2 ± 0.2 km s^{-1} (1 σ uncertainties).

4.3.2. H I Column Density

The interstellar H I column density along the line of sight to HZ 43A can be determined by three different means: fitting the spectral shape of the EUV continuum, fitting the damping wings of the H I Lyman-α profile, and fitting the converging Lyman series. This last method has the greatest uncertainties because the lines are typically all saturated, but for the low column density of this line of sight it is possible to obtain meaningful results.

Determination of the H I column density by analysis of the EUV spectrum of a star requires accurate knowledge of the stellar continuum flux. The EUV spectrum of a star is very sensitive to the presence of even trace quantitites of heavy elements in the photosphere, and substantial effort is usually required in order to model this spectrum accurately. HZ 43A is unusual in that no traces of heavy elements have yet been detected in its photosphere; hence it is not affected by this potential source of systematic error. *EUVE* spectra of HZ 43A have been analyzed by several groups, using different observations, different model atmosphere codes, and different fitting methods. The three most recent analyses of *EUVE* observations will be described briefly below.

Dupuis et al. (1995) analyzed observations from 1994 March 25,28 and 1994 May 20. They first determined the He I and He II column densities by fitting the ionization edges at 504Å and 228Å, respectively, and then determined the stellar T_{eff} and interstellar H I column density by fits over the 400–550Å bandpass. This wavelength range was chosen because it was least sensitive to variations in surface gravity or heavy element abundance. The fitting was done with model spectra computed from pure H model atmospheres (Vennes & Fontaine 1992). The results were $T_{eff} = 51100\,K \pm 500\,K$, and $N_{H I} = (8.7 \pm 0.6) \times 10^{17}\,cm^{-2}$ (1 σ). They also estimated that systematic uncertainties in the effective area of 20% would change T_{eff} by 3% and $N_{H I}$ by 10%. Uncertainties in the V magnitude (used to normalize the models) would have similar effects, but are small in

comparison. The ionization fraction of hydrogen was estimated by assuming that the ratio of total H to total He was 10:1, that there was no appreciable He III, and comparing the measured N_{HI} to the measured He I and He II column densities. The resulting ionization fraction for H, $f_H = N(H II) / N(H)$, was $< 0.4 \pm 0.1$.

Barstow et al. (1997) analyzed the 1994 May 20 observation also, but used H+He models computed by Koester (1991) and determined all stellar and ISM parameters from a simultaneous fit to the entire *EUVE* spectrum. The values for T_{eff} and $\log g$ were constrained to remain within the $1\,\sigma$ uncertainties of the values determined by Napiwotzki et al. (1993). The V magnitude used, 12.99, corresponds to model fluxes that are fainter by a factor of 1.077 than would be the case if the present best value of $V = 12.909$ were used (Bohlin 2000). This would result in an underestimate of the derived N_{HI} column density by a few percent. They performed fits with two classes of models: homogeneous H+He mixtures, and stratified compositions. The derived interstellar H I column densities and $1\,\sigma$ uncertainties were $N_{HI} = (8.8 \pm 0.2) \times 10^{17} \mathrm{cm}^{-2}$ (homogeneous) and $N_{HI} = 8.3^{+0.2}_{-0.1} \times 10^{17}\mathrm{cm}^{-2}$ (stratified). The difference between the results for the two models exceeds the statistical errors in the fits, indicating that systematic uncertainties in the nature of the appropriate model are significant. The ionization fraction was derived in the same manner as by Dupuis et al. (1995) to be $f_H = 0.19^{+0.15}_{-0.19}$ for homogeneous models, and $f_H = 0.22^{+0.11}_{-0.14}$ for stratified models. We have assumed that the results presented by Barstow et al. (1997) supercede the earlier results in Barstow et al. (1995), so we will not discuss the earlier results here.

Wolff et al. (1999) analyzed observations obtained 1997 June 25,26. They first fit the He I and He II ionization edges to determine the corresponding column densities, and then fit the full spectrum to determine the H I column density. The stellar spectrum was computed using the LTE model atmosphere code of Koester (1996), assuming a pure

hydrogen composition. The atmosphere parameters were not free, but fixed at values derived from fits to the Balmer lines. The values used for T_{eff} were $50800 \pm 300\,K$, and the corresponding column densities were $N_{HI} = 8.851^{+0.311}_{-0.300} \times 10^{17}\,cm^{-2}$. The uncertainties in the column densities are dominated by the uncertainty in the effective temperature (Wolff 2001, private communication). The V magnitude used to normalize the models was 12.89; this would overestimate the stellar flux by about 2% and would result in only a very slight overestimate of the H I column density. The ionization fraction was derived in the same manner as the previous two analyses to be $f_H = 0.03^{+0.10}_{-0.03}$.

An EUV spectrum of this star was also obtained by HUT and analyzed by Kimble et al. (1993) to derive $N_{HI} = (6.5 \pm 0.5) \times 10^{17}\,cm^{-2}$ ($1\,\sigma$ statistical errors; systematic uncertainties were estimated at 15–20% and are dominated by calibration uncertainties). This falls below the more recent *EUVE* determinations by approximately the combined random and systematic uncertainties. These uncertainties are considerably larger than those of the much higher signal-to-noise *EUVE* spectra, so we will not consider this measurement further. The three *EUVE* measurements described above will be addressed again at the end of this section.

We fit the GHRS spectrum of the interstellar H I plus D I Lyman-α profile towards HZ 43A to determine the properties of the neutral hydrogen in this direction. The spectrum was first scaled by a factor of 0.866 in order to match our model flux over the regions 1212.25 – 1213.25Å and 1218.0 – 1218.5Å. The spectrum was then normalized by an NLTE stellar model prior to fitting (see Section 4.1 for a description of the model). We found that additional normalization by a low-order polynomial was required to account for potential small wavelength–dependent errors in the flux calibration. The apparent photospheric radial velocity of HZ 43A (v_{ph}) was measured by Reid (1996) to be $+21\,km\,s^{-1}$. The spectrum and the model (shifted by $+21\,km\,s^{-1}$) are shown plotted in Figure 2. A visual inspection of the

figure shows that at least a linear polynomial will be required as an additional correction to the flux calibration.

No explicit uncertainty was given by Reid (1996) for the radial velocity, but it is probably about 10-15 km s^{-1}. We therefore examined the effects on the derived H$_I$ column density of varying this velocity. We created stellar models with the photospheric velocity set at zero, at the nominal value of +21km s^{-1}, and at ±5, ±10, ±15 km s^{-1} with respect to the nominal value. The GHRS Lyman-α spectrum was normalized by each model in turn, and the best fit to the spectrum was generated for fixed values of log N_{HI} ranging from 17.80 to 18.00 in steps of 0.01 dex. The resulting χ^2 contours are plotted in Figure 3. The Fe$_{II}$ and Mg$_{II}$ lines were fit simultaneously with the Lyman-α H$_I$ and D$_I$ line profiles. Because the Lyman-α profile extends over several Angstroms, it may be affected more by uncertainties in the flux calibration than are narrow lines. To investigate this possibility, we generated these χ^2 contours for continuum fits performed with both fourth-order and seventh-order polynomials. There was little correlation in either case between log N_{HI} and the photospheric velocity. For the fourth-order fits, the minimum χ^2 was obtained for a photospheric velocity of 26 km s^{-1}, but the χ^2 increased slowly for smaller velocities and increased rather steeply for higher velocities. For the seventh-order continuum fits, the minimum χ^2 was also at 26 km s^{-1}, but it increased rather rapidly for both lower and higher velocities. The H$_I$ column density and 2σ uncertainty derived was log $N_{HI} = 17.895^{+0.045}_{-0.035}$ from the fourth-order continuum fits, and log $N_{HI} = 17.905^{+0.045}_{-0.065}$ from the seventh-order fits. The corresponding χ^2 values were 2750 for 2871 degrees of freedom, and 2711 for 2868 degrees of freedom, respectively. Based on these fits, we have adopted the value log $N_{HI} = 17.90^{+0.05}_{-0.06}$ for our combined GHRS and *FUSE* datasets.

We examined the behavior of the continuum fits by varying the order of the polynomial from 1 to 8, for photospheric velocities (v_{ph}) of 0, +5, +11, +21, and +31 km s^{-1}, and

allowing the H I column density to vary freely in each fit. For velocities of 0 and +5 km s^{-1} there was relatively little effect of polynomial order on the reduced χ^2 (for orders > 1). For higher velocities the χ^2 improved significantly for orders up to 4 and improved only slightly thereafter (with minima at order 7), except that for +31 km s^{-1} the χ^2 dropped again for order 8. An examination of the polynomials in each case show that the dominant term gradually changes from linear at low v_{ph} to cubic at high v_{ph}, and that the amplitudes increase from $\pm$ 2% at low v_{ph} to $\pm$ 3% at higher v_{ph}. The higher-order terms gave slight improvements to the overall χ^2, but did not change the character of the continuum fits.

We evaluated the effects of the uncertainties of the background flux level on the derived log N_{HI}. Our best estimate of the background level at Lyman-α was 0.5% of the continuum flux level, obtained by letting the background be a free parameter in the fit. We then varied the background level by +2% and -2% of the continuum flux level, causing log N_{HI} to change by only $\pm$ 0.012.

We were unable to obtain a satisfactory fit to the observed Lyman-α profile with a single component of neutral material, but found that a good fit was possible only if a second, low-column density absorber were included. The temperature, column density, and relative velocity of this component were free parameters in the fits to the Lyman-α profile used to construct the χ^2 contours described above. For the fits in which the continuum was represented by fourth-order polynomials, the column density of this second component was log $N_{HI} = 14.9^{+0.3}_{-0.5}$ (2 σ). For the fits in which the continuum was represented by seventh-order polynomials, the column density of this second component was log $N_{HI} = 14.9^{+0.6}_{-0.2}$ (2 σ); We will adopt the value log $N_{HI} = 14.9^{+0.6}_{-0.5}$ (2 σ). The temperature of this component was 30,000 K $\pm$ 10,000 K (2 σ) for both cases. As the column density of the main H I component was increased, the derived column density for this second component would also increase, and its temperature would decrease. Similarly, as v_{ph} was increased, shifting

the NLTE core of the photospheric Lyman line closer to the red side of the saturated portion of the interstellar absorption profile, the column density of this second component would increase and the temperature would decrease. The heliocentric velocity of this component was found to be about -2.0 km s^{-1}, but as v_{ph} was varied from it would shift in the opposite direction (i.e. it would increase as v_{ph} decreased). We suggest that this low-column density, high-temperature H I component may be due to the "hydrogen wall" about the Solar System. The hydrogen wall is an accumulation of gas at the boundary of the heliosphere, where the solar wind and LISM interact. Hydrogen walls have been detected around the Sun along several lines of sight, and around several other stars (Wood & Linsky 1998; Linsky & Wood 1996; Wood et al. 2000). The gas in these walls is fairly hot, 30,000K - 180,000K, and H I column densities range from log $N_{HI} = 13.75$ to log $N_{HI} = 14.75$. The properties of the second H I component in our fits are consistent with these other detections. One potential problem with this interpretation, however, is that the Lyman-α profile observed for the similar high-latitude sightline to 31 Com ($l = 115°, b = +89°$) can be fit very well without any high-temperature component (Wood et al. 2000). The models of the interaction of the heliosphere and the LIC described by Wood et al. (2000) do predict absorption by such a hot component for the line of sight to 31 Com, so one possible explanation is that the LIC is inhomogeneous on small scales and that the corresponding conditions at the boundary of the heliosphere vary accordingly.

The best fit to the normalized Lyman-α profile, including the main component and the high-temperature component, is shown in Figure 4. The relative velocity of the main absorbing component matched that found for the D I, Mg II, and Fe II lines, about -5 km s^{-1}. This differs significantly from that expected for the local interstellar cloud (LIC), -8.8km s^{-1}, and the column density is much higher than would be expected from the LIC along this line of sight (log $N_{HI} = 16.47$; Redfield & Linsky (2000)). The velocity differs even more from that expected for the 'G' cloud, -12.1 km s^{-1}. The velocity is consistent,

however, with that found for the single absorber along the line of sight to 31 Com by Piskunov et al. (1997) (-4 ± 1 km s^{-1}). This absorber is called the North Galactic Pole cloud by Linsky et al. (2000, see their Figure 1).

The FUSE spectrum of the converging Lyman series might in principle be used to try to determine the H I column. Such fits give results consistent with the column density derived from the Lyman-α profile, but with rather large uncertainties. The main difficulty is that the flux calibration is inherently uncertain at precisely the wavelengths needed to perform the fits to the Lyman edge, because there is no reference star available for which unattenuated continuum flux is present at the Lyman edge. For any given set of parameters we find that the flux is overestimated at some wavelengths and underestimated at others, by about ±5%. If we allow for such uncertainties we find that variations of the gas Doppler b parameter within 1 σ limits result in variations in the derived log N_{HI} of about 0.15 dex, which is too large to provide a significant constraint on our results. Ultimately, we may be able to determine a more accurate calibration at these wavelengths by means of combining data from several white dwarfs for which reliable H I columns have been determined by other means. The interstellar H I absorption at the Lyman edge predicted from the column densities, temperatures, and turbulent velocity derived above from the GHRS data is shown in Figure 5. The agreement is excellent, indicating in particular that the Doppler width of the gas is accurately known. The effects of the broad component of the instrument LSF is clear in this Figure, as the flux in the cores of the saturated Lyman lines is several times higher than the background level seen below the Lyman edge.

We will combine the available *EUVE*–derived measurements of the H I column density with our GHRS / *FUSE* measurement to provide our best estimate of N$_{HI}$. The *EUVE* measurement uncertainties are driven in large part by the uncertainty in the effective temperature. Each group used different estimates for this uncertainty, but they show

similar sensitivity in the sense that a change in T_{eff} of 500K would correspond roughly to a change in N_{HI} of $0.6 \times 10^{17} cm^{-2}$ (this scaling is not apparent in the Barstow et al. 1997 paper, but in the earlier Barstow et al. 1995 paper N_{HI} appears to be roughly 50% more sensitive to changes in T_{eff}). If we take the uncertainty for T_{eff} from Dupuis et al. (1995) as representative, the corresponding uncertainty in N_{HI} from an individual *EUVE* measurement is roughly equal to the 1σ uncertainty in our determination of N_{HI} from the GHRS and FUSE data. Therefore, we will simply take the mean of the four measurements (after first averaging the two values obtained by Barstow et al. (1997) for both the homogeneous and stratified models), which gives $N_{HI} = 8.511 \times 10^{17} cm^{-2}$, or $\log N_{HI} = 17.930$. The standard deviation of the four values was 0.398×10^{17}, or 0.02 dex, but this may not be an adequate representation of the true uncertainty. Each of the EUV measurements is affected in a similar fashion by the uncertainties in the effective temperature. Barstow et al. (1997) were able to obtain relatively small uncertainties for N_{HI} in the context of either the homogeneous or stratified models, but the differences between the two corresponding column densities was $0.5 \times 10^{17} cm^{-2}$, or almost as much as for the nominal uncertainty of 500 K for T_{eff}. It is worth noting that the two recent optical determinations of T_{eff} have uncertainties greater than 500 K: 49000 ± 2000 K (3σ) by Napiwotzki et al. (1993) and 50822 ± 639 K (1σ) by Finley et al. (1997). Similarly, as we showed above in Section 2 the standard deviation for all the recent determinations of T_{eff} is about 700 K. Therefore, we prefer to use a somewhat more conservative estimate for the uncertainty in N_{HI}, and adopt the value $\log N_{HI} = 17.930 \pm 0.060$ (2σ).

4.3.3.   O I Column Density

The FUSE bandpass contains numerous O I absorption lines of varying strength. The total column density to HZ 43A is sufficiently low that even the strongest O I lines are close

to being on the linear part of the curve of growth. The data were analyzed with profile fits and a curve-of-growth analysis. Good quality data were obtained in all channels for the MDRS observation. Separate analyses of the day and night MDRS data actually give a somewhat higher value for N(O I) than the night data; the opposite would be expected if airglow contamination were significant.

The MDRS data were analyzed in 4 ways: the program Owens.f was used by two members of our group to perform independent profile fits, and a third member of our group performed both a profile fit using the code of Fitzpatrick (Spitzer & Fitzpatrick 1993) and a curve-of-growth analysis. Each analysis was performed with different choices of continuum regions to fit, different choices of polynomial order for the continuum fits, and different combinations of background level and LSF. The resulting column densities, with $2\,\sigma$ uncertainties, were: $\log N_{O I} = 14.47^{+0.07}_{-0.05}$, $\log N_{O I} = 14.48^{+0.08}_{-0.07}$, $\log N_{O I} = 14.50 \pm 0.04$, and $\log N_{O I} = 14.51^{+0.07}_{-0.06}$. The corresponding b-values and $2\,\sigma$ uncertainties from each fit were: 2.8 ± 0.2, 3, 2.5 ± 0.4, and 2.7 ± 0.3. The b-value for the second fit is poorly-determined because only unsaturated lines were included, which are insensitive to b. The first two b-values were from simultaneous fits to O I, N I, and N II lines in the *FUSE* data; if only the O I lines are included in the first fit the uncertainty increases to $\pm0.40\,\mathrm{km\ s^{-1}}$. The b-values fall somewhat below the value predicted from the line of sight velocity structure derived from the GHRS data, but are consistent within $2\,\sigma$. The above determinations are in good agreement with one another; we adopt the value $\log N_{O I} = 14.49 \pm 0.08$ $(2\,\sigma)$. A sample of the fits to the O I lines is shown in Figure 6, and the curve of growth is shown in Figure 7.

A number of tests were performed to examine the magnitude of the various possible systematic effects described in Section 4.2. Increasing the background level by a factor of 2 in the SiC channels and a factor of 4 in the LiF channels increased the value of $\log N_{O I}$

by 0.02 dex, decreasing the background by a factor of 2 decreased log N_{OI} by < 0.01 dex. Fitting only detector 1 data or only detector 2 data, to test for fixed-pattern noise effects and detector-dependent resolution or background effects, changed log N_{OI} by < 0.01 dex. Eliminating any single line from the fit, to test for erroneous f-values or fixed-pattern noise effects, had no effect on log N_{OI}. Eliminating both the line at 1039Å and the multiplet at 988Å from the first profile fit causes log N_{OI} to increase by 0.04 dex, but the uncertainty of the result doubles. Eliminating these lines from the COG analysis causes the resulting log N_{OI} to increase by only 0.02 dex. The LSF was varied by doubling the amplitude of the broad component, which increased log N_{OI} by 0.02 dex, and eliminating the broad component (with a corresponding increase in the background level to match the cores of the saturated Lyman lines), which decreased log N_{OI} by 0.02 dex. These effects have all been included in the uncertainties quoted above for the first profile fit.

4.3.4. NI Column Density

As with O I, the FUSE bandpass contains numerous N I absorption lines of varying strength. In this case the low column density to HZ 43A means that many of the lines that are ordinarily the most useful are not detected. High quality data were obtained in all channels in the MDRS observation, and usable data were obtained in all channels in the LWRS observation. We analyzed both the complete dataset and the pure night data for the LWRS observation and found that the geocoronal emission from N I during the day portion of the orbit did not significantly affect the absorption line profiles. The lines strong enough to be useful in the *FUSE* data were the triplet at 1134Å and the lines at 953.655Å and 953.970Å.

The MDRS data were analyzed by having two members of the group perform independent profile fits and a third member perform a curve-of-growth fit. The curve-of-

growth analysis also included the N I multiplet 1199.550Å, 1200.223Å, and 1200.710Å from the GHRS G160M dataset. For the MDRS data, the results were $\log N_{NI} = 13.51^{+0.05}_{-0.06}$, $\log N_{NI} = 13.51^{+0.06}_{-0.05}$, and $\log N_{NI} = 13.51^{+0.06}_{-0.05}$ (2 σ uncertainties). The b-value and 2 σ uncertainty derived from the curve of growth analysis was $3.0^{+1.4}_{-0.7}$km s^{-1}; no determination of b was possible from the profile fits because the lines used were all on the linear part of the curve of growth. The adopted value for $\log N_{NI}$ is 13.51 ± 0.06. The fit to the MDRS N I profiles is shown in Figure 8, and the curve of growth is shown in Figure 9.

The N I fits were subjected to the same tests for systematic errors as described in the previous section for O I. Because all of the N I lines in the *FUSE* band relatively weak, they are less sensitive to variations in the LSF or the background than partially saturated lines; none of these tests caused a variation in the $\log N_{NI}$ greater than 0.01 dex.

4.3.5. D I Column Density

Because of the low H I column density along this line of sight, absorption by D I is expected to be detectable at Lyman-α, Lyman-β, and possibly at Lyman-γ. The D I Lyman-α profile is shown in Figures 2 and 4; it is clearly well-resolved. The D I Lyman-β absorption is clearly seen in all *FUSE* channels in the MDRS observation, but is clearly detected only in the night portion of the LWRS observation in the LiF1 channel. The MDRS SiC2 Lyman-β spectrum was rather noisy, however, and was not included in the fits. D I Lyman-γ absorption is not detected in either SiC channel.

The GHRS Lyman-α profile was first fit independent of the *FUSE* data. The resulting value for the column density was $\log N_{DI} = 13.16 \pm 0.04$ (2 σ), with a b-value of 7.1 (implying the line is well-resolved by the GHRS echelle resolution). Changing the background level from our best estimate by ± 2% of the continuum level changed $\log N_{DI}$

by ±0.02 dex. A simultaneous fit to the GHRS Lyman-α spectrum and the *FUSE* MDRS

Lyman-β data from channels LiF1, LiF2, and SiC1 gave log $N_{DI} = 13.15 \, ^{+0.04}_{-0.045}$ ($2\,\sigma$).

Varying the fitting parameters for the *FUSE* data as described in Section 4.3.3 above for

O I resulted in variations in log N_{DI} of ±0.01. Profile fits to the *FUSE* MDRS data alone

gave log $N_{DI} = 13.11 \pm 0.20$. The LWRS LiF1 Lyman-β spectrum was not included in the

fits. The D I line is detected in this spectrum, and is consistent with the fits to the other

data, but the uncertain corrections for airglow contamination in the LWRS spectrum, even

for the night only data, means that these data will not significantly constrain the overall fit.

The *FUSE* D I line profiles are shown in Figure 10, along with the best fit to the combined

FUSE and GHRS datasets.

4.3.6. Other Species

A number of other species were detected in the ISM along the line of sight to HZ 43A.

These include C II, C III, N II, O VI, Si II, Ar I, and possibly N III in addition to the Mg II

and Fe II mentioned earlier. The column densities for these species are listed in Table 5.

Of particular interest is the column density for N II (log $N_{N II} = 13.62^{+0.13}_{-0.17}$), which slightly

exceeds that of N I. The ionization potential for N I is greater than that for H I, so ordinarily

one expects N to be predominantly neutral. The local ISM is dominated by hot gas that

may be far from ionization equilibrium, however, so estimates of the total abundance of

nitrogen in the local ISM must account for possible large ionization corrections to the

measured N I abundances. The N II transitions at 915.613Å and 1083.993Å are ordinarily

strongly saturated, but the total column density to HZ 43A is low enough that an accurate

N II column density can be determined. The N II absorption lines and best-fit line profiles

are shown in Figure 11. The N III column density quoted in Table 5 is an upper limit

because the N III 989.799Å is blended with the Si II 989.873Å line. If the Si II column density

derived from the 1193.290Å line and the b-value derived from O I are used to predict the equivalent width of the Si II 989.873Å line, then it is likely that at least half, and perhaps all, of the measured equivalent width at 989.8Å is caused by Si II rather than N III. Even if the measured absorption results primarily from N III, the upper limit suggests that N III is a minor contributor to the total N column along this sightline.

No H_2 was detected. The range of possible column densities was determined by using the profile-fitting program Owens to examine the regions of the spectrum in the vicinity of the two-dozen strongest H_2 absorption lines that were not blended with any other features. The column density of H_2 was then gradually increased until the change in chi-squared was unacceptable. The resulting $3 - \sigma$ upper limit to the column density of H_2 was 1.2×10^{13} cm^{-2}.

The column density for C II shown in Table 5 is larger than that for O I, possibly suggesting that C is over-abundant on this sightline, that O is depleted, or that there is substantial component of H II gas along this line of sight. The large column density of N II supports the latter explanation. It should be noted also that the column density for C II is particularly uncertain, because the saturation effects are large and depend on the assumption that the b-value for C II is the same as that of O I. If there is a substantial contribution to the column density from H II gas, the effective b-value for C II will likely be larger than that for O I and the C II column density will be overestimated accordingly. This source of systematic error is not included in the uncertainties quoted in Table 5; the column density derived from the apparent optical depth method ($\log N(C II) = 13.63$) is a reasonable lower limit.

We note that C II* at 1037.018 Å is not detected in our *FUSE* observations. The 3σ upper limit to the equivalent width of this line in the LiF1A data is $W_\lambda \leq 5.5$ mÅ, including a crude estimate of the continuum placement uncertainties. This implies $\log N(C II^*) \lesssim 12.7$

(3σ) along the HZ 43A sight line. If one assumes the excitation of C II* is due to electrons, the electron density may be calculated by comparing the column densities of the excited- and ground-state C II:

$$n_e \approx 0.18 \frac{N(\text{C II}^*)}{N(\text{C II})} T^{1/2}$$

(see Spitzer & Fitzpatrick 1993). Assuming $T = 5353$ K (see Section 4.3.1) and that $\log N(\text{C II}) = 14.83$ (derived using the O I b-value), we find $n_e \lesssim 0.1$ cm^{-3}. Given the uncertainties in the latter assumption, however, a more conservative value is $n_e \ll 1.5$ cm^{-3}, derived using the lower limit for the C II column density determined with the apparent optical depth method.

5. Summary

The line of sight to HZ 43A was investigated using a combination of *FUSE* spectra, archival GHRS spectra, and results obtained from *EUVE* spectra taken from the literature. The line of sight to HZ 43A is particularly simple, with only a single velocity component discernible. An additional high-temperature component was found with a very low column density, detectable only in H I. The line of sight to HZ 43A exits the LIC after a very short distance, and the velocity of the main component of the absorbing gas is not compatible with the velocity of the nearby G cloud in the LISM, hence this material is presumed to be located in the North Galactic Pole cloud. Doppler widths for each species determined from profile fits or curve of growth analyses of the *FUSE* data were consistent with the temperature and turbulent velocity for the gas derived from the GHRS high resolution data. Consistent fits to the D I column density were obtained when fitting the *FUSE* and GHRS data separately and simultaneously, indicating that the D I Lyman-α line is not affected by saturation effects. The *FUSE* spectra were used to determine O I and D I column densities by both profile fitting and curve of growth analyses, with consistent results obtained in each

case. Careful attention was paid to numerous potential sources of systematic error. Our adopted H I column density, log N_{HI} = 17.93 ± 0.06 (2 σ), is the mean of our measurement from the GHRS Lyman-α profile and the EUV measurements of Dupuis et al. (1995), Barstow et al. (1997), and Wolff et al. (1999).

Our results are summarized in Table 6. All uncertainties in the table are 2 σ (but values quoted below from the literature are 1 σ). Our result for D/H along the line of sight to HZ 43A is (1.66 ± 0.28) × 10^{-5}. The GHRS dataset analyzed in this work has been previously analyzed by Landsman et al. (1996), who obtained the similar value for D/H of 1.6 × 10^{-5}. Our value for D/H along this sightline exceeds by approximately 1.5 σ both the mean value reported by Linsky (1998) for measurements of D/H within 100 pc of the sun, (1.47 ± 0.10) × 10^{-5}, and the mean value of the *FUSE* measurements reported in this first set of papers (Moos et al. 2001).

Our result for O I/H I is (3.63 ± 0.84) × 10^{-4}. Converting this ratio to a logarithmic abundance log (O I/H I) + 12.00 gives $8.56^{+0.09}_{-0.11}$. The ionization balance for both O and H are linked by resonant charge exchange reactions (see Jenkins et al. 2000 and references therein), and there is no apparent H_2 present, so O I/H I should be representative of O/H along this line of sight. Meyer et al. (1998) report an average gas-phase abundance for 13 sight lines of (3.43 ± 0.15) × 10^{-4} (after correction for our preferred O I λ1355 oscillator strength of $f = 1.16 \times 10^{-6}$ from Welty et al. 1999), and they estimate no more than O/H$\sim$ 1.8 × 10^{-4} can be incorporated into grains, implying an upper limit to the total (gas+dust) ISM oxygen abundance of 5.2 × 10^{-4}. Our O/H measurement is consistent with the average gas-phase value of Meyer et al. (1998).

Sofia & Meyer (2001b,a) have demonstrated that the value of O/H determined from F and G star photospheres, (4.45 ± 1.56) × 10^{-4}, is consistent with two recent determinations of the solar abundance, (5.45 ± 1.00) × 10^{-4} (Holweger 2001) and $(4.90^{+0.60}_{-0.53}) \times 10^{-4}$ (Allende

Prieto et al. 2001), and with the total oxygen abundance estimated from the work of Meyer et al. (1998). Sofia & Meyer (2001b,a) argue that the recent solar system values should therefore be used as the ISM abundance standard for oxygen. Our value for O/H in the gas phase along the line of sight to HZ 43A is significantly lower than each of these values, although not by more than 2 σ (given the large uncertainties in the solar system determinations). Our result is in agreement with the compilation of B-star abundances presented by Sofia & Meyer (2001b,a), $(3.50 \pm 1.33) \times 10^{-4}$, although these authors argue that B-star abundances are unlikely to be appropriate measures of the ISM standard. It seems likely that the gas-phase oxygen abundance measured by Meyer et al. (1998) implies modest depletion of oxygen in the ISM towards more distant stars; given the agreement of our O/H measurement with the Meyer et al. average, it seems likely a similar degree of oxygen depletion is present in the cloud observed along the HZ 43A sight line.

The ionization fractions for N and H are not as strongly coupled as those of O and H (Jenkins et al. 2000), so it is possible for N to be more highly ionized than H, and therefore for the gas-phase abundance of N relative to its solar system value to be less than that of O. If we combine our column densities for N I, N II, and the maximum likely column density for N III (assuming only half of the measured absorption is due to Si II), we obtain a total nitrogen column density of $N_N = 7.88^{+1.56}_{-1.43} \times 10^{13}$, and a ratio N/H I $= (9.26 \pm 1.87) \times 10^{-5}$. This ratio provides an upper limit to N/H, corresponding to the limit that that hydrogen along this line of sight is predominantly neutral. Given the significant column density of N II, it is reasonable to expect that there will also be a significant column density of H II present. Converting to a logarithmic scale with log $N_{HI} = 12.00$ gives an abundance for N of $7.97^{+0.08}_{-0.10}$. This is consistent with the solar abundance value of Grevesse & Noels (1993), 7.97, and the more recent value from Holweger (2001) of 7.93 ± 0.11, and somewhat exceeds the value of 7.81 for nearby B stars (Gies & Lambert 1992). We can set a lower limit to the N abundance by setting the ionization fraction of H to the upper limit of 50% found

by Dupuis et al. (1995) (the other *EUVE* analyses obtained lower ionization fractions for hydrogen). The resulting logarithmic abundance is $7.79^{+0.08}_{-0.10}$, essentially equal to the value for B stars, and consistent with the ISM gas phase abundance of Meyer et al. (1997). Thus N is not significantly depleted onto dust grains along this line of sight.

Further discussion of the implications of these results and comparisons with other sightlines can be found in the companion paper by Moos et al. (2001).

REFERENCES

Allende Prieto, C., Lambert, D. L., & Asplund, M. 2001, ApJ, 556, L63

Barstow, M. A., Dobbie, P. D., Holberg, J. B., Hubeny, I., & Lanz, T. 1997, MNRAS, 286, 58

Barstow, M. A., Holberg, J. B., & Koester, D. 1995, MNRAS, 274, L31

Bohlin, R. C. 2000, AJ, 120, 437

Bohlin, R. C., Colina, L., & Finley, D. S. 1995, AJ, 110, 1316

Burles, S. 2000, Nuclear Physics A, 663, 861

Cardelli, J. A. & Ebbets. D. C. 1994, in Calibrating Hubble Space Telescope, ed. J. C. Blades & S. J. Osmer (STScI/ST-ECF), 322

Cardelli, J. A., Ebbets, D. C., & Savage, B. D. 1993, ApJ, 413, 401

Cardelli, J. A., Savage, B. D., & Ebbets, D. C. 1990, ApJ, 365, 789

Clark, L. L. & Dolan, J. F. 1999, A&A, 350, 1085

Cox, D. P. & Reynolds, R. J. 1987, ARA&A, 25, 303

Dahn, C. C., Harrington. R. S., Riepe, B. Y., Christy, J. W., Guetter, H. H., Kallarakal, V. V., Miranian, M., Walker, R. L., Vrba, F. J., Hewitt, A. V., Durham, W. S., & Ables, H. D. 1982 AJ, 87, 419

Dupuis, J., Vennes, S., Bowyer, S., Pradhan, A. K., & Thejll, P. 1995, ApJ, 455, 574

Dupuis, J., Vennes, S., Chayer, P., Hurwitz, M., & Bowyer, S. 1998, ApJ, 500, L45

Epstein, R. I., Lattimer, J. M., & Schramm, D. N. 1976, Nature, 263, 198

Finley, D. S., Koester, D., & Basri, G. 1997, ApJ, 488, 375

Friedman, S. D., Howk, J. C., Chayer, P., Tripp, T. M., Hébrard, G., Andre, M., Oliveira, C., Jenkins, E. B., Moos, H. W., Sonneborn, G., Lemontagne, R., Oegerle, W. R., & Sembach, K. R. 2001, ApJ, submitted

Frisch, P. C. 1995, Space Science Reviews, 72, 499

Gies, D. R. & Lambert, D. L. 1992, ApJ, 387, 673

Grevesse, N. & Noels, A. 1993, in Origin of the Elements, ed. N. Prantzos, E. Vangioni-Flam, & M. Casse (Cambridge University Press), 15–25

Hébrard, G., Lemoine, M., Desert, J.-M., Vidal-Madjar, A., Lecavelier des Etangs, A., Ferlet, R., Wood, B. E., Linsky, J. L., Kruk, J. W., Chayer, P., Lacour, S., Blair, W. P., Friedman, S. D., Moos, H. W., Oegerle, W. R., Sembach, K. R., & Sonneborn, G. 2001, ApJ, submitted

Holberg, J. B., Basile, J., & Wesemael, F. 1986, ApJ, 306, 629

Holweger, H. 2001, in Solar and Galactic Composition, ed. R. F. Wimmer-Schweingruber (Berlin: Springer)

Howk, J. C., Savage, B. D., & Fabian, D. 1999, ApJ, 525, 253

Howk, J. C., Sembach, K. R., Roth, K. C., & Kruk, J. W. 2000, ApJ, 544, 867

Hubeny, I. & Lanz, T. 1995, ApJ, 439, 875

Jenkins, E. B. 1986, ApJ, 304, 739

Jenkins, E. B., Oegerle, W. R., Gry, C., Vallerga, J., Sembach, K. R., Shelton, R. L., Ferlet, R., Vidal-Madjar, A., York, D. G., Linsky, J. L., Roth, K. C., Dupree, A. K., & Edelstein, J. 2000, ApJ, 538, L81

Kimble, R. A., Davidsen, A. F., Long, K. S., & Feldman, P. D. 1993, ApJ, 408, L41

Koester, D. 1991, in IAU Symp. 145: Evolution of Stars: the Photospheric Abundance Connection, Vol. 145, 435

Koester, D. 1996, in IAU Colloq. 152: Astrophysics in the Extreme Ultraviolet, 185

Kruk, J. W., Brown, T. M., Davidsen, A. F., Espey, B. R., Finley, D. S., & Kriss, G. A. 1999, ApJS, 122, 299

Kruk, J. W., Kimble, R. A., Buss, R. H., Davidsen, A. F., Durrance, S. T., Finley, D. S., Holberg, J. B., & Kriss, G. A. 1997, ApJ, 482, 546

Landsman, W., Sofia, U. J., & Bergeron, P. 1996, in Science with the Hubble Space Telescope – II, ed. P. Benvenuti, F. D. Machetto, & E. J. Schreier (STScI/ST-ECF)

Lehner, N., Gry, C., Sembach, K. R., Hébrard, G., Chayer, P., Moos, H. W., Howk, J. C., & Desert, J.-M. 2001, ApJ, submitted

Lemke, M. 1997, A&AS, 122, 285

Lemoine, M., Audouze, J., Ben Jaffel, L., Feldman, P., Ferlet, R., Hébrard, G., Jenkins, E. B., Mallouris, C., Moos, W., Sembach, K., Sonneborn, G., Vidal-Madjar, A., & York, D. G. 1999, New Astronomy, 4, 231

Lemoine, M., Vidal-Madjar, A., Hébrard, G., Desert, J.-M., Ferlet, R., Lecavelier des Etangs, A., Howk, J. C., Andre, M., Blair, W. P., Friedman, S. D., Kruk, J. W., Lacour, S., Moos, H. W., Oegerle, W. R., Sembach, K. R., Chayer, P., Jenkins, E. B., Koester, D. Wood, B. E., Linsky, J. L., Sonneborn, G., & York, D. 2001, ApJ, submitted

Linsky, J. L. 1998, Space Science Reviews, 84, 285

Linsky, J. L., Redfield, S., Wood, B. E., & Piskunov, N. 2000, ApJ, 528, 756

Linsky, J. L. & Wood, B. E. 1996, ApJ, 463, 254

Margon, B., Liebert, J., Lampton, M., Spinrad, H., Bowyer, S., & Gatewood, G. 1976, ApJ, 209, 525

Meyer, D. M., Cardelli, J. A., & Sofia, U. J. 1997, ApJ, 490, L103

Meyer, D. M., Jura, M., & Cardelli, J. A. 1998, ApJ, 493, 222

Moos, H. W., Cash, W. C., Cowie, L. L., Davidsen, A. F., Dupree, A. K., Feldman, P. D., Friedman, S. D., Green, J. C., Green, R. F., Gry, C., Hutchings, J. B., Jenkins, E. B., Linsky, J. L., Malina, R. F., Michalitsianos, A. G., Savage, B. D., Shull, J. M., Siegmund, O. H. W., Snow, T. P., Sonneborn, G., Vidal-Madjar, A., Willis, A. J., Woodgate, B. E., York, D. G., Ake, T. B., Andersson, B. ., Andrews, J. P., Barkhouser, R. H., Bianchi, L., Blair, W. P., Brownsberger, K. R., Cha, A. N., Chayer, P., Conard, S. J., Fullerton, A. W., Gaines, G. A., Grange, R., Gummin, M. A., Hébrard, G., Kriss, G. A., Kruk, J. W., Mark, D., McCarthy, D. K., Morbey, C. L., Murowinski, R., Murphy, E. M., Oegerle, W. R., Ohl, R. G., Oliveira, C., Osterman, S. N., Sahnow, D. J., Saisse, M., Sembach, K. R., Weaver, H. A., Welsh, B. Y., Wilkinson, E., & Zheng, W. 2000, ApJ, 538, L1

Moos, H. W., Sembach, K. R., Friedman, S. D., Hébrard, G., Kruk, J. W., Lehner, N., Sonneborn, G., Vidal-Madjar, A., Wood, B. E., Blair, W. P., Dupree, A. K., Jenkins, E. B., Linsky, J. L., Oegerle, W. R., Savage, B. D., Shull, J. M., & York, D. G. 2001, ApJ, submitted

Morton, D. C. 1991, ApJS, 77, 119

Napiwotzki, R., Barstow, M. A., Fleming, T., Holweger, H., Jordan, S., & Werner, K. 1993, A&A, 278, 478

Napiwotzki, R., Green, P. J., & Saffer, R. A. 1999, ApJ, 517, 399

Piskunov, N., Wood, B. E., Linsky, J. L., Dempsey, R. C., & Ayres, T. R. 1997, ApJ, 474, 315

Redfield, S. & Linsky, J. L. 2000, ApJ, 534, 825

Reid, I. N. 1996, AJ, 111, 2000

Sahnow, D. J., Moos, H. W., Ake, T. B., Andersen, J., Andersson, B. ., Andre, M., Artis, D., Berman, A. F. Blair, W. P., Brownsberger, K. R., Calvani, H. M., Chayer, P., Conard, S. J., Feldman, P. D., Friedman, S. D., Fullerton, A. W., Gaines, G. A., Gawne, W. C., Green, J. C., Gummin, M. A., Jennings, T. B., Joyce, J. B., Kaiser, M. E., Kruk, J. W., Lindler, D. J., Massa, D., Murphy, E. M., Oegerle, W. R., Ohl, R. G., Roberts, B. A., Romelfanger, M. L., Roth, K. C., Sankrit, R., Sembach, K. R., Shelton, R. L., Siegmund, O. H. W., Silva, C. J., Sonneborn, G., Vaclavik, S. R., Weaver, H. A., & Wilkinson, E. 2000, ApJ, 538, L7

Savage, B. D., Edgar, R. J., & Diplas, A. 1990, ApJ, 361, 107

Savage, B. D. & Sembach, K. R. 1991, ApJ, 379, 245

Schramm, D. N. & Turner, M. S. 1998, Reviews of Modern Physics, 70, 303

Sembach, K. R. 2000, Atomic and Molecular Data for Astrophysics: New Developments, Case Studies and Future Needs, 24th meeting of the IAU, Joint Discussion 1, August 2000, Manchester, England., 1, E18

Sembach, K. R. & Savage, B. D. 1992, ApJS, 83, 147

Sfeir, D. M., Lallement, R., Crifo, F., & Welsh, B. Y. 1999, A&A, 346, 785

Sofia, U. J. & Meyer, D. M. 2001a, ApJ, 558, L147

—. 2001b, ApJ, 554, L221

Sonneborn, G., Andre, M., Oliveira, C., Hébrard, G., Howk, J. C., Tripp, T. M., Chayer, P., Friedman, S. D., Kruk, J. W., Jenkins, E. B., Moos, H. W., Oegerle, W. R., Sembach, K. R., & Vidal-Madjar, A. 2001, ApJ, submitted

Spitzer, L. 1978, Physical processes in the interstellar medium (New York Wiley-Interscience, 1978. 333 p.)

Spitzer, L. J. & Fitzpatrick, E. L. 1993, ApJ, 409, 299

van Altena, W. F., Lee, J. T., & Hoffleit, E. D. 1995, The General Catalog of Trigonometric Stellar Parallaxes (New Haven: Yale University Observatory)

Vennes, S. 1992, ApJ, 390, 590

Vennes, S. & Fontaine, G. 1992, ApJ, 401, 288

Vennes, S., Thejll, P., & Shipman, H. L. 1991, in NATO ASIC Proc. 336: White Dwarfs, 235

Vennes, S., Thejll, P. A., Galvan, R. G., & Dupuis, J. 1997, ApJ, 480, 714

Vidal, C. R., Cooper, J., & Smith, E. W. 1973, ApJS, 25, 37

Welty, D. E., Hobbs, L. M., Lauroesch, J. T., Morton, D. C., Spitzer, L., & York, D. G. 1999, ApJS, 124, 465

Wesemael, F., van Horn, H. M., Savedoff, M. P., & Auer, L. H. 1980, ApJS, 43, 159

Wolff, B., Koester, D., & Lallement, R. 1999, A&A, 346, 969

Wood, B. E. & Linsky, J. L. 1998, ApJ, 492, 788

Wood, B. E., Linsky, J. L , Hébrard, G., Vidal-Madjar, A., Lemoine, M. Moos, H. W., & Sembach, K. R. 2001, ApJ, submitted

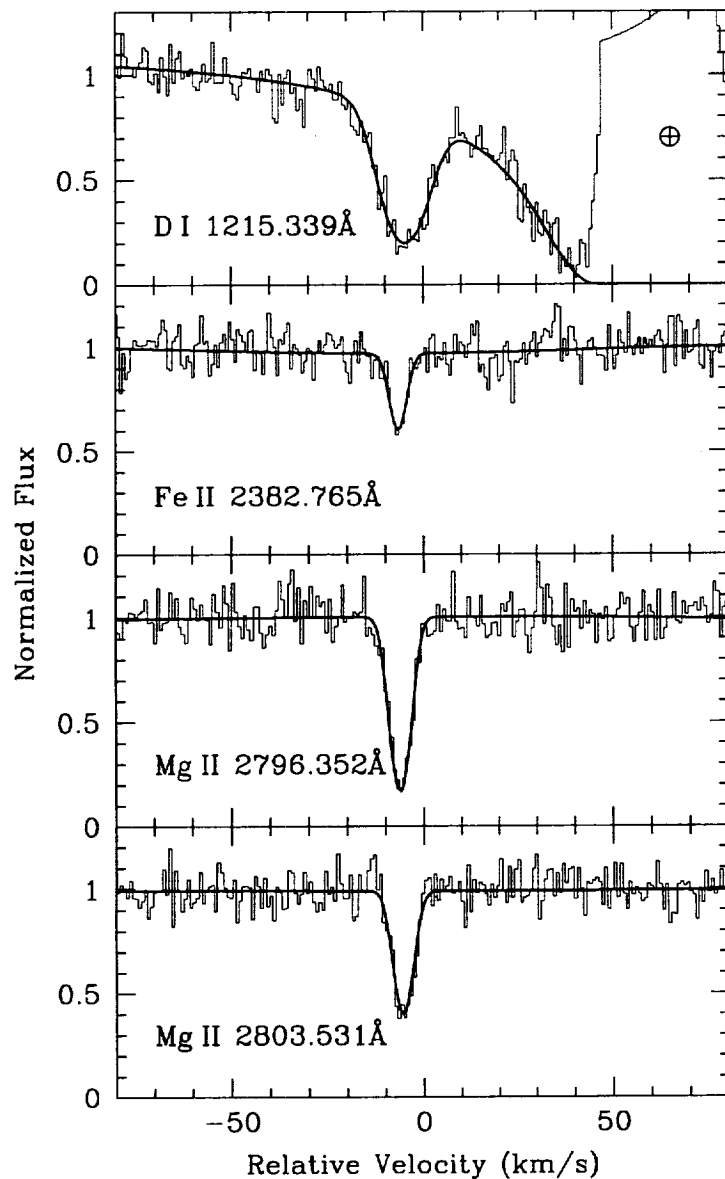Wood, B. E., Müller, H., & Zank, G. P. 2000, ApJ, 542, 493

Fig. 1.— Absorption profiles of D I, Fe II, and Mg II are plotted as a function of heliocentric velocity. The histograms are the GHRS echelle measurements, and the smooth line is the single-component fit. No evidence for a second velocity component is seen. The D I line sits on the broad wing of the interstellar H I Lyman-α profile; the truncated peak at $+65$ km s^{-1} in the D I plot is geocoronal Lyman-α emission.
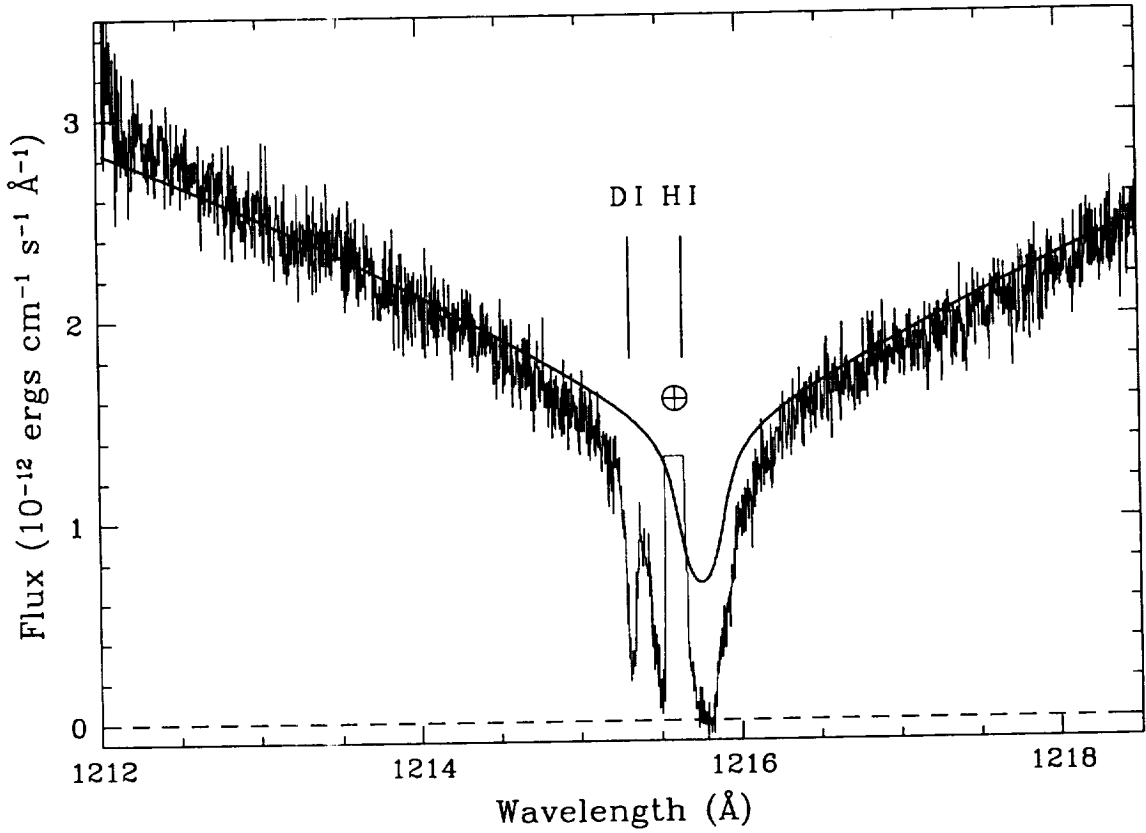
Fig. 2.— The GHRS echelle spectrum of the Lyman-α profile is shown as the histogram, the stellar model as the smooth curve. The model is shifted to a heliocentric velocity of +21 km s^{-1}. The positions of the interstellar H I and D I absorption lines are marked. The truncated peak at 1215.6Å marked with an earth symbol is geocoronal H I Lyman-α emission. The GHRS spectrum was normalized to match the mean flux of the model over the regions 1212.25Å-1213.25Å and 1218.0Å-1218.5Å; additional low-order polynomial corrections were applied to the continuum flux when fitting (see text). The zero level is shown as the dashed line.
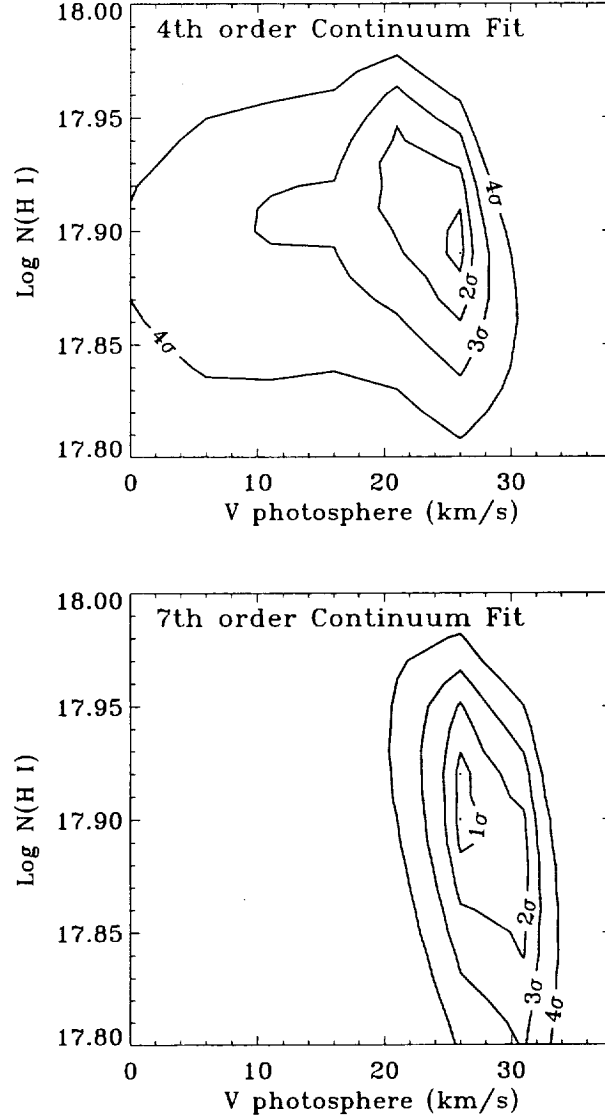
Fig. 3.— Plots of the χ^2 contours are shown for fits to the GHRS Lyman-α profile as a function of log $N_{H\,I}$ and photospheric velocity. The top plot shows the results for 4th order polynomial continuum fits, and the bottom plot shows the results for 7th order polynomial continuum fits.
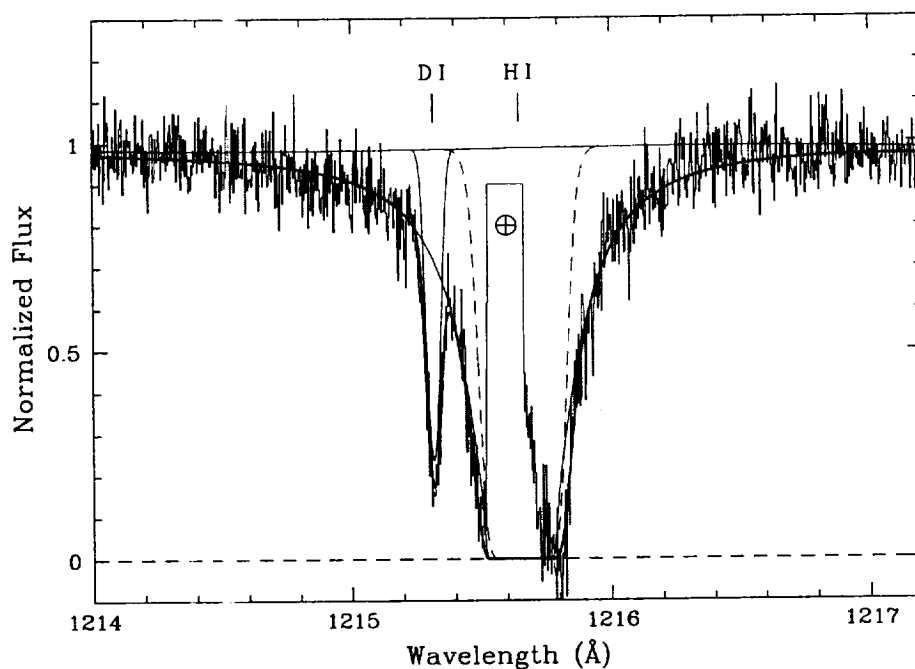
Fig. 4.— The normalized GHRS spectrum of the Lyman-α profile is shown as the histogram, and the best fit is shown as the smooth curve. The thin curves show the continuum fit and the individual H I and D I profiles; the dashed curve shows the low-column density high-temperature H I component; and the thick solid line shows the overall fit. The stellar model in this fit was shifted to a heliocentric velocity of $26 \, \text{km s}^{-1}$, which provided slightly better fits than the nominal value of $21 \, \text{km s}^{-1}$. The positions of the interstellar H I and D I absorption lines are marked. The truncated peak at 1215.6Å marked with an earth symbol is geocoronal H I Lyman-α emission. The zero level is shown as a dashed line.
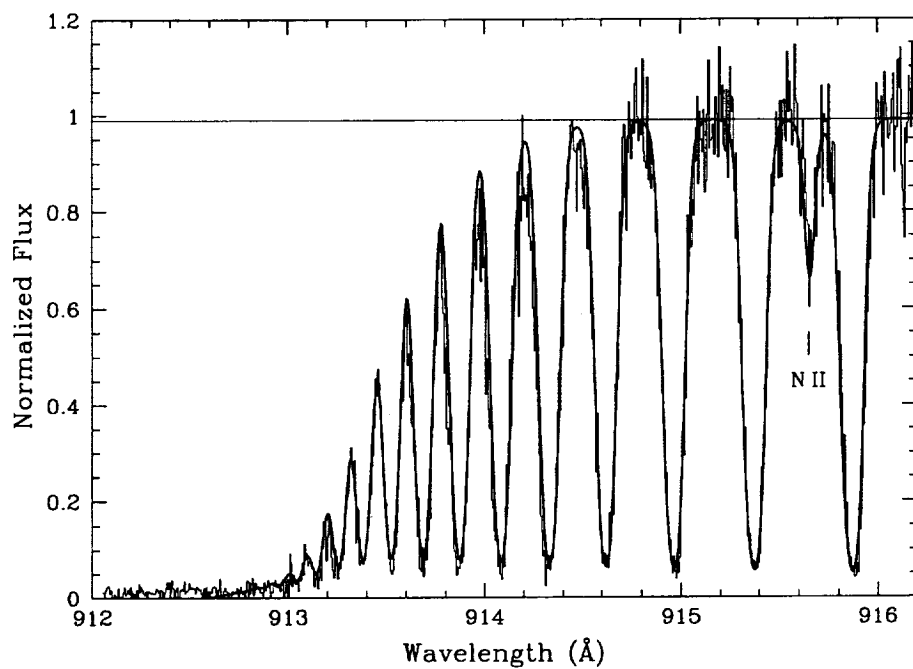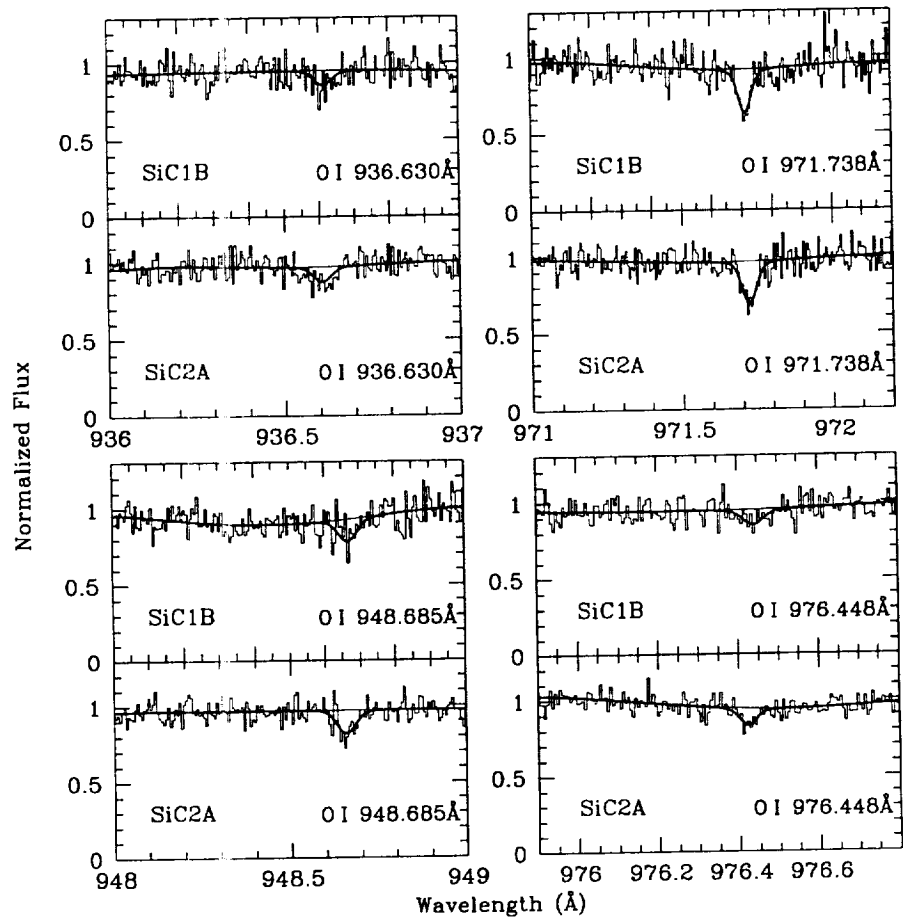
Fig. 5.— The *FUSE* MDRS SiC1b spectrum of the converging H I Lyman series is plotted as the histogrammed points, the profiles resulting from the best fit to the Lyman-α profile as the smooth line. The assumed continuum is shown as the thin solid line. The LWRS spectrum is essentially identical, but with lower signal to noise.
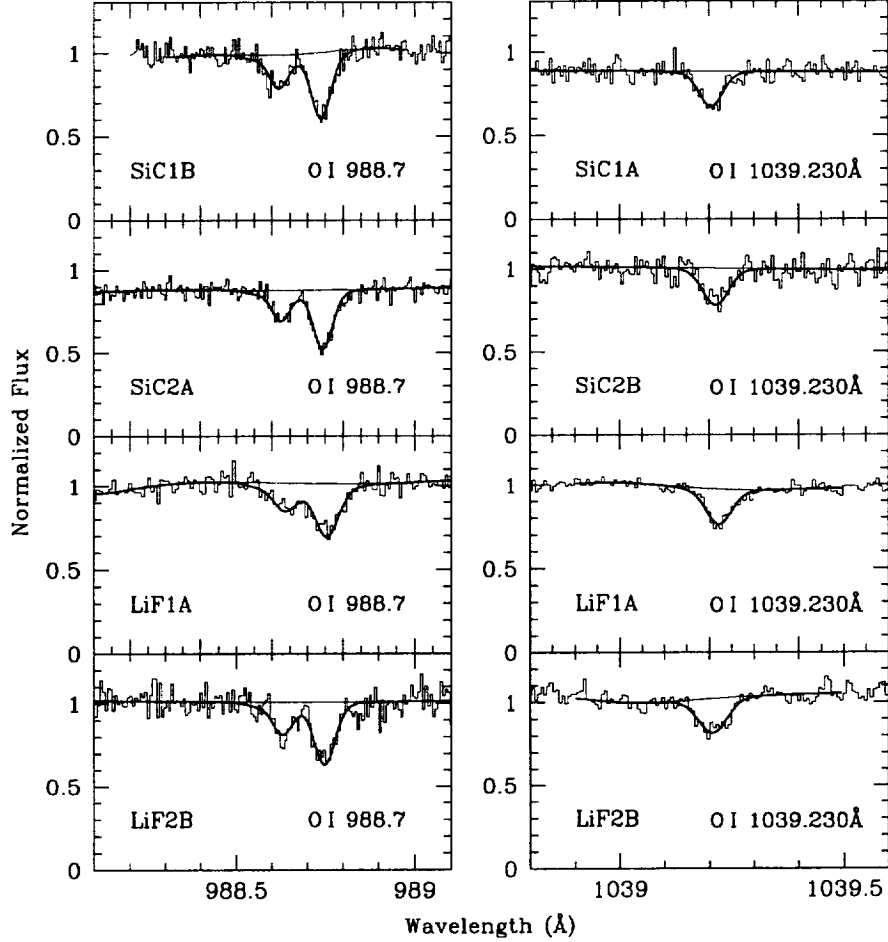
Fig. 6.— The observed *FUSE* MDRS O I line profiles are shown as the histogrammed data points, the continuum fits are the thin solid lines, and the profiles computed from the adopted O I column density and doppler width is plotted as the thick solid curve. The data are unbinned.
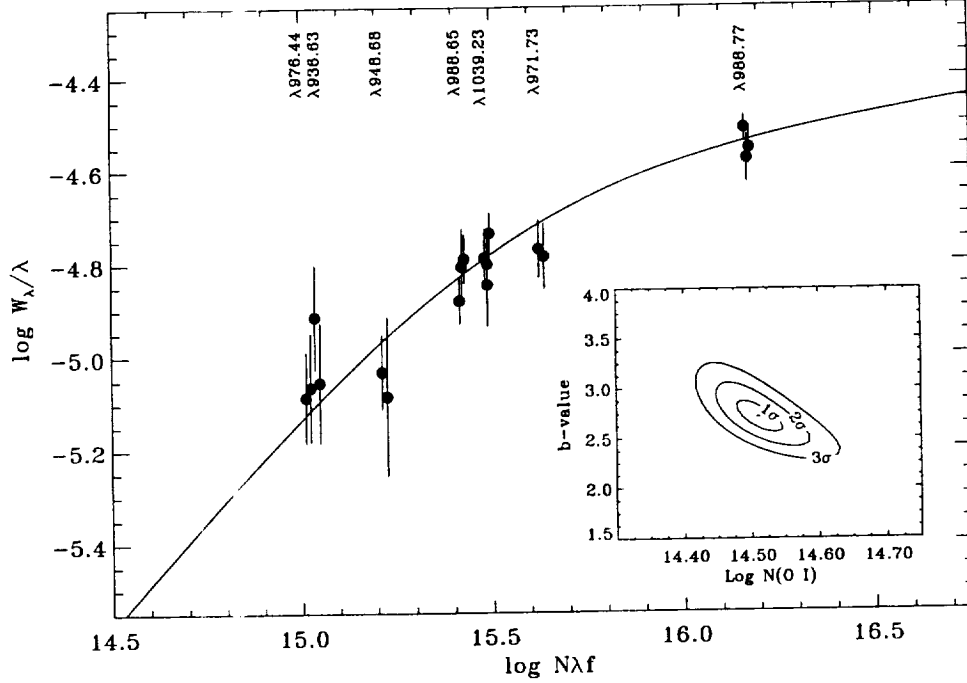
Fig. 7.— The equivalent widths of O I lines measured from FUSE MDRS data are plotted, along with the best-fit curve of growth (b = 2.72 km s^{-1}). The inset shows contours of constant $\Delta\chi^2$ in the b–log N plane. The measurements of lines from multiple channels have been offset slightly in log Nλf to avoid confusion. The wavelengths of the lines are marked along the top of the figure. The plotted errorbars indicate the 1σ measurement uncertainties in the equivalent widths.

Fig. 8.— The FUSE MDRS N I line profiles are shown as the thin histogram and the best fit is shown as the thick solid line. The continuum fit is the thin smooth line. The SiC data have been binned by two pixels for plotting purposes.
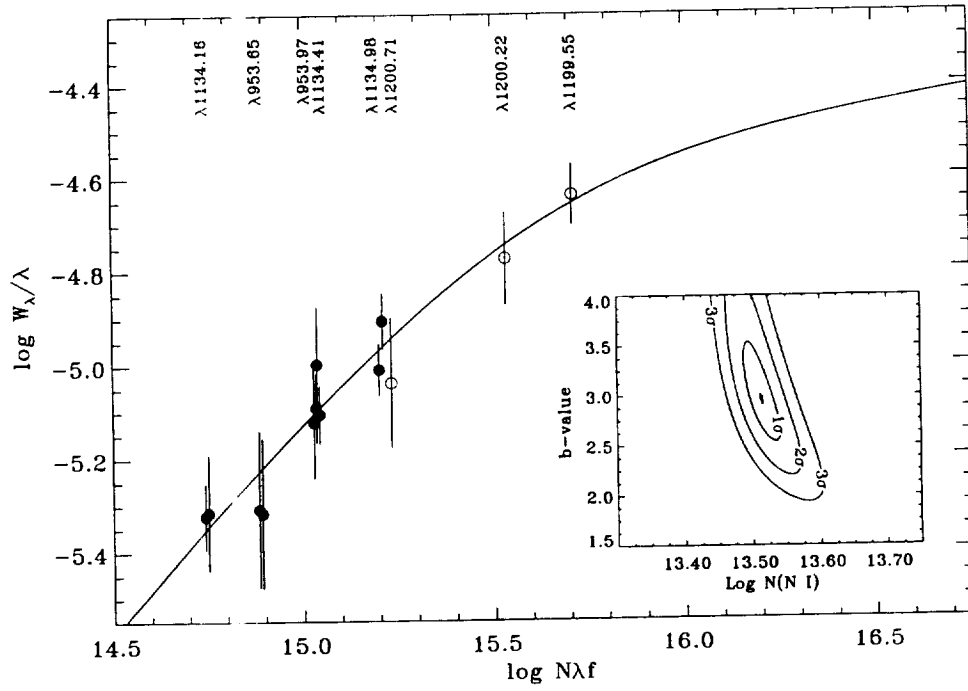
Fig. 9.— As for Figure 7, but for N I. The solid circles are from FUSE MDRS data, the open circles from intermediate-resolution GHRS spectra.
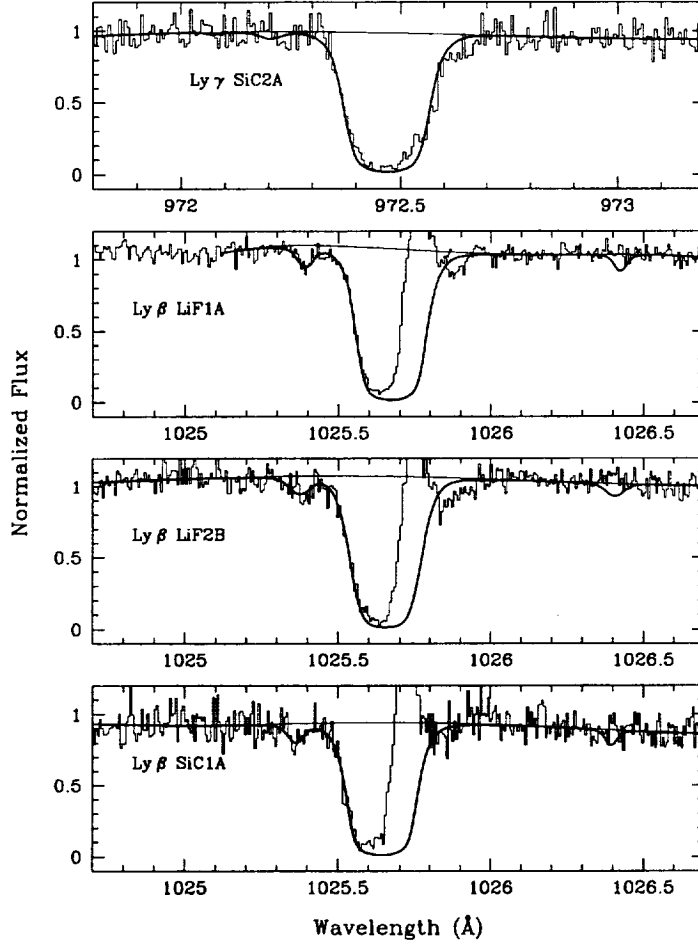
Fig. 10.— The FUSE spectra of H I and D I Lyman-β and Lyman-γ absorption are plotted as the thin histogram, and the best fit to the combined GHRS and *FUSE* data as the thick smooth line. No D I absorption is seen at Lyman-γ, but it is clearly seen at Lyman-β. The geocoronal Lyman-β emission is clearly seen in the red wing of the interstellar absorption; it is well-separated from D I. Geocoronal emission at Lyman-γ is present, but quite weak. The O I 1026.473Å absorption predicted from the measured O I column density is also plotted; no absorption is seen at this wavelength so it has been assumed that the oscillator strength for this line is in error. It was not included in any fits.
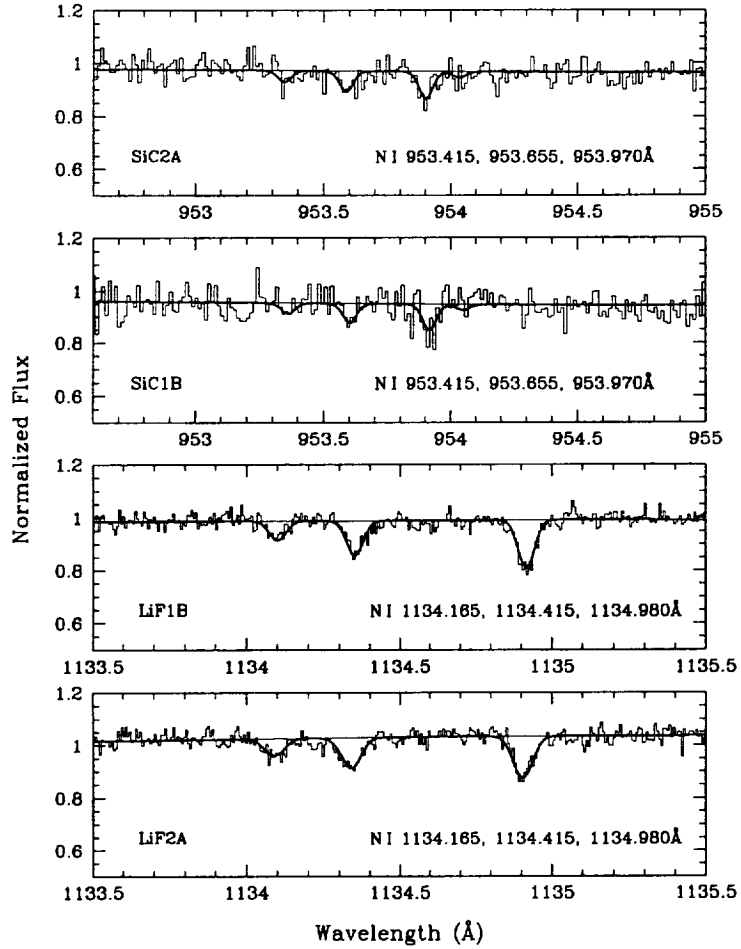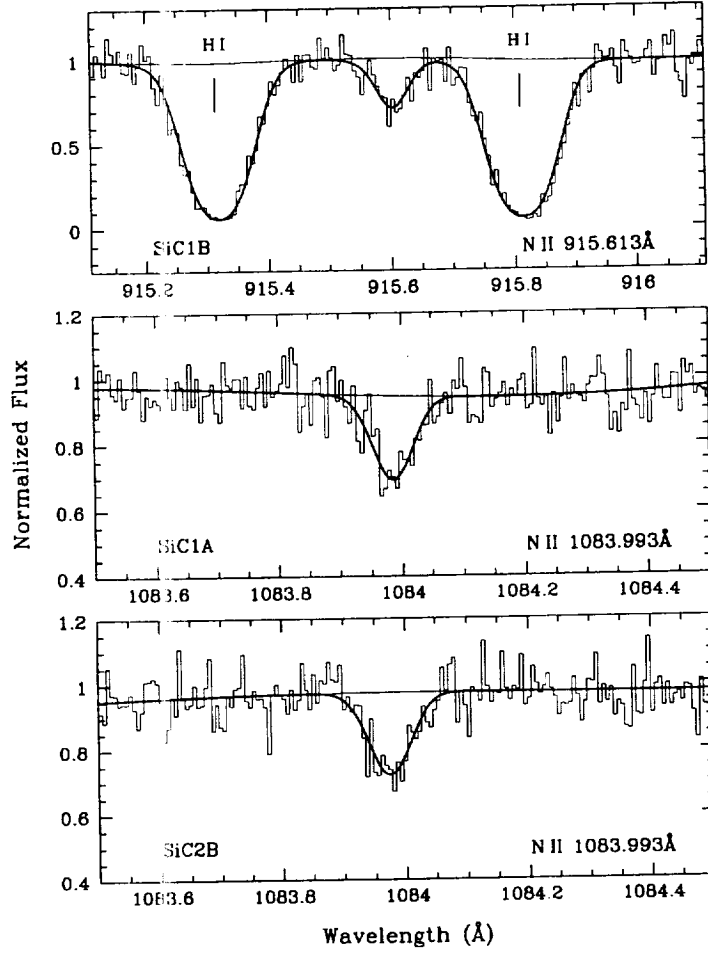
Fig. 11.— The FUSE MDRS N II line profiles are shown as the thin histogram and the best fit is shown as the thick solid line. The continuum fit is the thin smooth line. The neighboring interstellar H I line profiles are labelled with tick marks in the plot of the 915.663Åline.

Table 1.   Target Summary for HZ 43A

Quantity	Value	Reference
Spectral Type	DA1	1
α_{2000}[a]	$13^h16^m21\!\!.\!\!^s78$	2
δ_{2000}[a]	$+29°05'55\!\!.\!\!''5$	2
l	$54.11°$	2
b	$+84.16°$	2
d[b] (pc)	68 ± 13	3
V	12.914	2
$B - V$	-0.31	2
T_{eff} (K)	50,900	1
$\log g$ (cm s^{-2})	8.0	1

[a]Corrected for proper motion to epoch 2000.5

[b]Trigonometric parallax

References. — (1) Finley et al. 1997; (2) Bohlin et al. 1995; (3)van Altena et al. 1995.

– 61 –

Table 2. Log of *FUSE* observations.

Dataset ID	Aperture	Obs date	T_{exp} (total)[a]	T_{exp} (night)[a]	N_{exp}[b]
M1010501	LWRS	Feb 19 2000	6092	2333	8
P1042301	LWRS	Apr 22 2000	14447	5136	23
P1042302	MDRS	Feb 08 2001	39606	20572	85

[a]Exposure duration in seconds.

[b]Number of individual exposures.

Table 3.   Log of GHRS observations.

Dataset ID	Grating and order	Aperture and substep pattern	Wavelength range Å	Start Time (UT)[a]	Exposure Time (s)
Z2R50104T	Ech A - 46	LSA 7	1212-1218	00:21	7834
Z2R50107T	Ech A - 46	LSA 7	1212-1218	05:05	7181
Z2R50204T	Ech B - 24	LSA 7	2376-2387	09:59	2176
Z2R50205T	Ech B - 20	LSA 7	2791-2807	11:27	2176
Z2R50209T	G160M	SSA 5	1192-1228	13:10	1414

[a]All exposures began on July 30 1995.

Table 4. Equivalent Width Measurements

Species	$\lambda_c{}^a$	$\log \lambda f^b$	Channel	W_λ [mÅ]^c	S/N^d
			FUSE		
C II	1036.337	2.088	LiF1A	$37.8^{+1.7}_{-2.7}$	42
			LiF2B	$39.8^{+2.2}_{-2.8}$	26
			SiC1A	$39.4^{+2.2}_{-2.4}$	19
C III	977.020	2.870	SiC1B	$14.6^{+3.1}_{-2.2}$	16
			SiC2A	$15.6^{+1.7}_{-1.5}$	22
N I	953.655	1.376	SiC1B	$4.6^{+2.2}_{-1.9}$	15
			SiC2A	$4.7^{+2.3}_{-2.1}$	17
N I	953.970	1.521	SiC1B	$9.6^{+3.9}_{-2.3}$	16
			SiC2A	$7.2^{+1.9}_{-2.6}$	20
N I	1134.165	1.238	LiF1B	$5.5^{+1.7}_{-1.9}$	47
			LiF2A	$5.4^{+1.0}_{-0.9}$	47
N I	1134.415	1.528	LiF1B	$8.9^{+1.7}_{-1.0}$	46
			LiF2A	$9.2^{+1.5}_{-1.9}$	43
N I	1134.980	1.693	LiF1B	$14.1^{+1.6}_{-2.5}$	46
			LiF2A	$11.1^{+1.2}_{-1.8}$	43

Table 4—Continued

Species	$\lambda_c{}^a$	$\log \lambda f^b$	Channel	$W_\lambda \ [\text{mÅ}]^c$	S/N^d
N II	915.613	2.180	SiC1B	$20.3^{+4.7}_{-3.4}$	13
N II	1083.994	2.097	SiC2B	$23.3^{+3.0}_{-3.1}$	14
N III	989.799	2.085	SiC2A	$< 8.2^{+2.9}_{-1.7}{}^e$	25
O I	936.630	0.534	SiC1B	$8.3^{+2.9}_{-2.7}$	13
			SiC2A	$11.4^{+4.6}_{-2.1}$	15
O I	948.685	0.778	SiC1B	$7.8^{+4.8}_{-2.7}$	12
			SiC2A	$8.8^{+1.9}_{-1.6}$	15
O I	971.738	1.123^f	SiC1B	$15.9^{+2.6}_{-3.0}$	10
			SiC2A	$16.5^{+2.5}_{-2.5}$	13
O I	976.448	0.509	SiC1B	$8.4^{+2.7}_{-2.4}$	15
			SiC2A	$8.0^{+2.0}_{-2.0}$	18
O I	988.655	0.914	SiC1B	$16.0^{+2.2}_{-1.9}$	20
			SiC2A	$13.0^{+1.7}_{-1.4}$	23
			LiF2B	$15.4^{+3.6}_{-2.7}$	14
O I	988.773	1.662	SiC1B	$27.5^{+2.1}_{-2.7}$	20
			SiC2A	$30.4^{+1.6}_{-2.2}$	24
			LiF2B	$26.1^{+3.5}_{-3.0}$	14

Table 4—Continued

Species	$\lambda_c{}^a$	$\log \lambda f^b$	Channel	W_λ [mÅ]^c	S/N^d
O I	1039.230	0.980	LiF1A	$19.1^{+1.7}_{-2.2}$	42
			LiF2B	$16.9^{+2.9}_{-2.2}$	26
			SiC1A	$16.4^{+2.2}_{-2.9}$	19
O VI	1031.926	2.137	LiF1A	$8.5^{+2.1}_{-1.7}$	39
			LiF2B	$8.4^{+2.7}_{-2.1}$	25
Ar I	1048.220	2.442	LiF1A	$2.2^{+1.2}_{-0.8}$	49
			LiF2B	$< 2.4\ (2\sigma)$	25

GHRS

Species	$\lambda_c{}^a$	$\log \lambda f^b$	Channel	W_λ [mÅ]^c	S/N^d
N I	1199.550	2.192	G160M	$27.6^{+4.2}_{-4.6}$	17
N I	1200.223	2.015	G160M	$20.2^{+5.8}_{-4.4}$	17
N I	1200.710	1.713	G160M	$11.0^{+4.3}_{-4.0}$	16
Mg II	2796.352	3.236	Ech-A	55^{+3}_{-3}	12
Mg II	2803.531	2.933	Ech-A	$37.9^{+2.2}_{-2.2}$	13
Si II	1193.290	2.775	G160M	$24.7^{+7.0}_{-4.9}$	16

Table 4—Continued

Species	λ_c[a]	$\log \lambda f$[b]	Channel	W_λ [mÅ][c]	S/N[d]
Fe II	2382.765	2.882	Ech-A	$20.5^{+2.3}_{-2.3}$	12

[a]Central wavelength of each transition from Morton 2001.

[b]Adopted product of wavelength and oscillator strength for each transition, taken from Morton 2001.

[c]Measured equivalent width and 1σ uncertainties (in mÅ). The uncertainties contain contributions from both statistical and systematic error sources.

[d]Empirically estimated signal-to-noise ratios (per unbinned pixel) for continuum regions near the absorption lines of interest.

[e]The N III absorption contains a substantial contribution from Si II at 989.873 ($\approx +21$ km s^{-1} from the center of the N III line). The equivalent width quoted may be dominated by the latter, but represents a firm upper limit for the amount of N III along the HZ 43A sight line.

[f]This transition is a blend of three O I lines, the sum of whose oscillator strengths are given here.

Table 5. Curve of Growth Column Densities

Species	$\log N \pm 2\sigma$ [a]	$b \pm 2\sigma$ [b]	$\Delta \log N$ [c]
C II	$14.83^{+0.17}_{-0.34}$	[d],[e]	+1.20
C III	$12.59^{+0.09}_{-0.10}$	[d]	+0.15
N I	$13.51^{+0.06}_{-0.05}$	$3.0^{+1.4}_{-0.7}$	$\cdots$
N II	$13.62^{+0.13}_{-0.17}$	[d]	+0.32
N III	$< 12.98^{+0.22}_{-0.25}$	[d]	+0.07
O I	$14.51^{+0.07}_{-0.06}$	$2.72^{+0.33}_{-0.26}$	$\cdots$
O VI	$12.91^{+0.08}_{-0.08}$	∞ [f]	$\cdots$
Si II	$12.85^{+0.18}_{-0.22}$	[d]	+0.21
Ar I	$11.96^{+0.30}_{-0.50}$	[d]	+0.00
Mg II	12.41 ± 0.02	2.8 ± 0.3	$\cdots$
Fe II	12.17 ± 0.04	2.78 ± 1.15	$\cdots$

[a]Log of column density derived from a curve of growth fit, with estimated 2σ uncertainties. For most species not enough transitions were observed to independently fit a curve of growth and determine a b-value. In these cases we have adopted the b-value of $2.72^{+0.33}_{-0.26}$ (2σ) from O I.

[b]Doppler parameter in km s^{-1} with estimated 2σ uncertainties.

[c]For those species for which we have adopted the b-value from O I we give the amount by which the curve-of-growth-corrected column density given in column 2 of this table exceeds the average integrated apparent column den-

Table 6.   HZ 43 Column Densities and Ratios[a]

	H I	D I	O I	N I
Log N	17.93 ± 0.06	$13.15^{+0.040}_{-0.045}$	14.49 ± 0.08	13.51 ± 0.06
Ratios				

D I/H I	O I/H I	N I/H I	D I/O I	D I/N I
$1.66 \pm 0.28 \times 10^{-5}$	$3.63 \pm 0.84 \times 10^{-4}$	$3.80 \pm 0.74 \times 10^{-5}$	$4.57 \pm 0.96 \times 10^{-2}$	$4.37 \pm 0.74 \times 10^{-1}$

[a]all uncertainties are 2σ